

1 **Trends of the high latitude mesosphere temperature and mesopause**
2 **revealed by SABER**

3 **Xiao Liu^{1,2}, Jiyao Xu^{2,3}, Jia Yue^{4,5}, Yangkun Liu^{1,2}, and Vania F. Andrioli^{2,6}**

4 ¹Institute of Electromagnetic Wave, School of Physics, Henan Normal University, Xinxiang,
5 453000, China

6 ²State Key Laboratory of Space Weather, National Space Science Center, Chinese Academy of
7 Sciences, Beijing, 100190, China

8 ³School of Astronomy and Space Science, University of the Chinese Academy of Science, Beijing,
9 100049, China

10 ⁴Catholic University of America, Washington, DC 20064, USA

11 ⁵NASA Goddard Space Flight Center, Greenbelt, MD, 20771, USA

12 ⁶Heliophysics, Planetary Science and Aeronomy Division, National Institute for Space Research
13 (INPE), Sao Jose dos Campos, Sao Paulo, Brazil

14

15 *Correspondence to: Jiyao Xu (xujy@nssc.ac.cn)*

16

17 **Key Points:**

- 18 • The mean temperature in the high latitude MLT region is obtained by binning the SABER
19 observations based on yaw cycles during 2002–2023
- 20 • In the high latitude MLT, the cooling trend is seasonal symmetric and reaches peak of ≥ 6
21 K/decade at highest latitudes around summer solstice
- 22 • The trends of mesopause temperature depend on latitudes but are mostly negative and have
23 larger magnitudes at highest latitude

24

25

26 **Abstract**

27 The temperature trend in the mesosphere and lower thermosphere (MLT) region can be
28 regarded as an indicator of climate change. Using temperature profiles measured by the Sounding of
29 the Atmosphere using Broadband Emission Radiometry (SABER) instrument during 2002–2023
30 and binning them based on yaw cycle, we get continuous dataset with wide local time coverage at
31 50°S–80°N or 80°S–50°N. The seasonal change of temperature, caused by the forward drift of
32 SABER yaw cycle, is removed by using the climatological temperature of MSIS2.0. The corrected
33 temperature without any waves is regarded as the mean temperature. At 50°S–50°N, the cooling
34 trends of the mean temperature are significant in the MLT region and are in agreement with
35 previous studies. The novel finding is that the cooling trends of ≥ 2 K/decade exhibit seasonal
36 symmetric and reach peaks of ≥ 6 K/decade at high latitudes around the summer solstice. Moreover,
37 there are warming trends of 1–2.5 K/decade at altitude range of 10^{-2} – 10^{-3} hPa, specifically at
38 latitudes higher than 55°N in October and December and at latitudes higher than 55°S in April and
39 August. The mesopause temperature (altitude) in the northern summer polar region is colder (lower)
40 than that in the southern counterpart by ~ 5 – 11 K (~ 1 km) over the past 22 years. The trends of the
41 mesopause temperature are dependent on latitudes and months. But they are negative at most
42 latitudes and reach larger magnitudes at high latitudes. These results indicate that the temperature in
43 the high latitude MLT region is more sensitive to dynamic changes.

44

45 **1 Introduction**

46 Observational and simulation studies have revealed that the global mean temperature trend is
47 cooling in the mesosphere and lower thermosphere (MLT) (Beig et al., 2003; Laštovička et al.,
48 2006; Yue et al., 2019b; Laštovička, 2023). The cooling trends observed in the MLT region are
49 mainly caused by the increasing anthropogenic greenhouse gases such as carbon dioxide. Moreover,
50 changes of the stratospheric ozone depletion and recovery, increasing mesospheric water vapor
51 concentration, solar and geomagnetic variations may also contribute to the long-term changes of
52 temperature in the MLT region (Laštovička, 2009; Yue et al., 2019a, 2015; Garcia et al., 2019;
53 Mlynczak et al., 2022; Zhang et al., 2023).

54 A recent review work by Laštovička (2023) summarized that temperature trends are generally
55 cooling but also depend on local times, heights, and geographic locations in the MLT region
56 (Venkat Ratnam et al., 2019; Das, 2021; She et al., 2019; Yuan et al., 2019; Ramesh et al., 2020).
57 These results were mostly derived from ground-based and satellite observations at low and middle
58 latitudes, while the simulations provided insights into the long-term trends from pole to pole. On the
59 other hand, the long-term trends in temperature at high latitudes have not been thoroughly examined
60 and well understood yet, due to scarce observations. Driven by the summer-to-winter meridional
61 circulation, the upwelling causes adiabatic cooling in the summer polar mesosphere, while the
62 downwelling causes adiabatic warming in the winter polar mesosphere (Dunkerton, 1978; Garcia
63 and Solomon, 1985). Thus, the high latitude temperature is more sensitive to the changes of
64 dynamics, wave and forcing, stratospheric wind etc. (Russell et al., 2009; Qian et al., 2017; Yu et
65 al., 2023).

66 The progress in studying long-term trends in the MLT region has been summarized and
67 reported by Laštovička and Jelínek (2019) and Laštovička (2023). Here we highlight some studies
68 related to the temperature trends at high latitudes. Using temperature measured by the Sounding of
69 the Atmosphere using Broadband Emission Radiometry (SABER) instrument and simulated by
70 Whole Atmosphere Community Climate Model version 4 (WACCM4), Garcia et al. (2019) showed
71 that the global mean SABER temperature (52°S – 52°N) had cooling trends of 0.4–0.5 K/decade
72 during 2002–2018 in the stratosphere and mesosphere. These magnitudes were smaller than those
73 simulated by WACCM4 (0.6–0.9 K/decade) but within 2 times of the standard deviation. Using
74 Leibniz Institute Middle Atmosphere Model (LIMA) under northern hemispheric conditions during
75 1871–2008, Lübken et al. (2018) showed that the cooling trend in the MLT region was 1.5 K/decade
76 during 1960–2008, and was 0.7 K/decade during 1871–2008 at 55 – 61°N on geometric heights.
77 However, the trend was neglectable on pressure heights. On pressure heights, the global mean
78 SABER temperature (55°S – 55°N) had cooling trends of 0.5 and 2.6 K/decade, respectively, at 10^{-3}
79 hPa (~ 92 km) and 10^{-4} hPa (~ 106 km) during 2002–2021 (Mlynczak et al., 2022). The results of

80 Lübken et al. (2018) and Mlynczak et al. (2022) illustrated that the cooling trends were larger over
81 recent decades on both geometric and pressure heights as compared to the beginning of
82 industrialization. To achieve a longer time series, Li et al. (2021) constructed a nearly 30-year
83 dataset at 45°S–45°N by merging the temperature measured by the Halogen Occultation Experiment
84 (HALOE) instrument during 1991–2005 and the SABER instrument during 2002–2019. They
85 showed that the cooling trend was significant and reached a peak of 1.2 K/decade at 60–70 km in
86 the Southern Hemisphere (SH) tropical and subtropical region. Moreover, the cooling trend in the
87 SH was larger than its counterpart in the Northern Hemisphere (NH).

88 At high latitudes, ground-based observations of OH nightglow rotational temperature revealed
89 a significant cooling trend of 1.2 ± 0.51 K/decade at Davis (68°S, 78°E) during 1995–2019 (French
90 et al., 2020). The OH rotational temperature around midnight exhibited a significant cooling trend
91 of $2.4 \text{ K} \pm 2.3$ /decade in summer and an insignificant cooling trend of 0.4 ± 2.2 K/decade in winter
92 at Moscow (57°N, 37°E) during 2000–2018 (Dalin et al., 2020). Using the ice layer parameters
93 simulated by the LIMA model and the Mesospheric Ice Microphysics And transport ice particle
94 model, Lübken et al. (2021) showed that the negative trend of noctilucent clouds altitudes (~83 km)
95 was primarily caused by the increasing CO₂ in the troposphere during 1871–2008 at 58°N, 69°N,
96 and 78°N. At these three latitudes, the cooling trends were of ~0.2 K/decade during 1871–1960 and
97 1.0 K/decade during 1960–2008. Near the latitude band of 64–70°N in June and 64–70°S in
98 December, Bailey et al. (2021) constructed two datasets by merging the temperature measured by
99 HALOE and SABER and by HALOE and SOFIE (Solar Occultation for Ice Experiment). They
100 showed that there were cooling trends of ~1–2 K/decade near 0.1–0.01 hPa (~68–80 km) and
101 warming trends of ~1 K/decade near 0.005 hPa (~85 km) at 64–70°N in June and 64–70°S in
102 December. Moreover, the WACCM-X simulation results by Qian et al. (2019) showed that the
103 temperature trends were mostly cooling in the MLT region. However, there were also warming at
104 ~80–95 km in the SH polar region from November to February (Fig. 3 of their paper). The
105 disagreement of these results at high latitudes might attribute to the different temporal spans and
106 local times, observations using different instruments, and different methods deriving the trends. It is
107 overarching to study the temperature trends at high latitudes using one coherent measurement over a
108 long period.

109 The SABER temperature profiles cover latitudes of 53°S–83°N in the north viewing
110 maneuvers and 83°S–53°N in the south viewing maneuvers since 2002. The operational SABER
111 temperature profile covers an altitude range of ~15–110 km. The precision and systematic
112 erroruncertainties of SABER temperature profile are height dependent. For a single temperature
113 profile, its precisionsuncertainties are summarized at
114 <https://spdf.gsfc.nasa.gov/pub/data/timed/saber/> and are of ~~-1.8–2.3 K~~ 1.8 K at 80 km, 3.6 K at

115 ~~90km, 6.7 K at 100 km, and 15.0 K at $z=60-80$ km, $\sim 5.4-8.4$ K at $90-100$ km, and $\sim 8.4-29.2$ K~~
116 ~~at $100-110$ km~~ under the condition of vertical resolution of 2 km. Moreover, for a single
117 temperature profile, its systematic errors defined by one standard deviation (corresponding to the
118 confidence level of 68%) are of ~ 1.4 K at and below 80 km, 4.0 K at 90 km, 5.0 K at 100 km, and
119 25.0 K at 110 km for typical midlatitude condition (Remsberg et al., 2008; Rezac et al., 2015;
120 Dawkins et al., 2018). The systematic errors will be doubled if they are defined by two times of
121 standard deviation (corresponding to the confidence level of 95%). These data exhibited remarkable
122 stability over the last two decades following the correction of algorithm instability (Mlynczak et al.,
123 2020, 2022, 2023). Using the SABER temperature profiles during 2002–2019, Zhao et al. (2020)
124 employed a 60-day moving window to obtain the mean temperature. Their analysis revealed that the
125 annual and global mean trend of mesopause temperature is cooling with magnitude of 0.75
126 K/decade. Moreover, the cooling trend is significant in non-summer seasons but insignificant in
127 summer (May–August) at $60-80^\circ\text{N/S}$. It should be noted that, SABER yaw cycle (YC) drifted
128 forward about one month from 2002 to 2023 (see Fig. 1 below) due to changing satellite orbit. This
129 induces the local time (LT) coverage in a certain month differing from year to year at high latitudes
130 if the window is set to be constantly 60-day.

131 Here we focus on the trend of the mean temperature without any atmospheric waves (i.e.,
132 gravity waves, tides and planetary waves). Calculating zonal mean can remove gravity waves,
133 nonmigrating tides and long-period planetary waves. However, migrating tides depend on LT and
134 are strong in the MLT region. They cannot be simply removed by calculating zonal mean. In this
135 work, we bin the data based on YC, which covers an interval of 54–64 days (see Fig. 1 below) and
136 provides almost full local time coverage (except the 1–3 hours around noon). Thus, the mean
137 temperature can be accurately determined by removing the migrating tides at $53^\circ\text{S}-83^\circ\text{N}$ or $83^\circ\text{S}-$
138 53°N using harmonic fitting. Each YC at every year covers varying ranges of dates. This results in
139 the aliasing of the seasonal variation of temperature into the mean temperature of each YC. This
140 issue can be resolved as below. We use the temperature of the recently released whole-atmosphere
141 empirical model MSIS2.0 (Emmert et al., 2021) as a reference for the seasonal variation. This
142 seasonal variation (more than 10 K as seen in Fig. 2b) embedded in YC drift is removed from the
143 mean temperature of each YC. Thus, using the advantages of SABER measurements at high
144 latitudes and binning the data based on YC, we focus on the long-term trends of the mean
145 temperature and the mesopause in the high latitude MLT region.

146 **2 Method of calculating mean temperature and trend**

147 The mean temperature (\bar{T}_{bk}) excludes gravity wave, tides and planetary waves. Moreover,
148 compared to the magnitudes of \bar{T}_{bk} , its trend is a small value and should be determined with extra

149 caution. The method of calculating \bar{T}_{bk} is based on a YC window. This ensures a good LT coverage
 150 at high latitudes. Compared to the fixed 60-day window, the advantage and necessity of the YC
 151 window are described below.

152 The YC window is defined as the temporal interval during which the SABER measurements
 153 are in the northward or southward viewing maneuver. Figure 1 shows the beginning date and
 154 temporal span of each YC. We see that there are about six YCs in each year, being named as YC1–
 155 YC6. The temporal spans of YCs are 54–64 days. This ensures that the LT coverage of SABER
 156 samplings is more than 18 hours at high latitudes. Therefore, migrating tides can be removed
 157 efficiently through harmonic fitting. In contrast, the LT coverage in a fixed 60-day window is
 158 different from year to year at high latitudes. This is because the temporal span of each YC drifted
 159 forward about one month from 2002 to 2023 (Fig. 1). For the case of the fixed 60-day window and
 160 at 70°N and in March (spanning from 14th February to 14th April with a center on 15th March), the
 161 sampling hours distributed at 0–2, 5–11, and 21–24 LT and had a coverage of only 14 hours in
 162 2005. However, the sampling hours in 2022 distributed at 0–10 and 13–24 LT and had a coverage of
 163 22 hours. The year-to-year variations of LT distribution and coverage might induce uncertainties
 164 and biases into \bar{T}_{bk} . Thus, the YC dependent window is necessary to obtain a wide LT coverage.

165

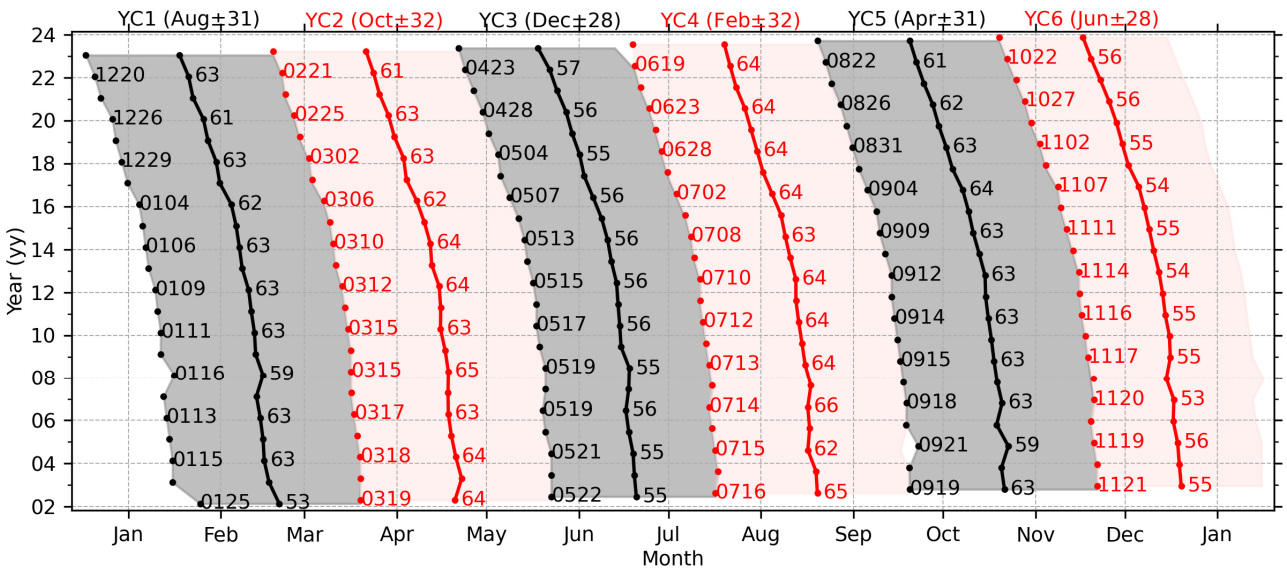


Figure 1. The temporal span of each YC from 2002 to 2023. The gray (red) region indicates the north (south) viewing maneuver. The beginning date (format of “mmdd”, “mm” and “dd” mean the month and the day of month, respectively) and temporal span (unit of days) of each yaw are labeled on the right of beginning (dot) and center date (dot-line), respectively. The six YCs and their center date in 2003 and half spans and are labeled as YC1–YC6 on the top.

166

167 We note that the forward drift of YC raises an issue that each YC at every year covers varying

168 ranges of date. This aliases seasonal variation of temperature into \bar{T}_{bk} and should be removed to get
 169 a corrected mean temperature (\bar{T}_{bcrt}). The detailed procedure of the calculating \bar{T}_{bcrt} and its trend is
 170 presented in Sec. 2.1–2.3. The procedure of calculating mesopause temperature and height is
 171 presented in Sec. 2.4.

172 2.1 Removing waves from SABER temperature

173 In each YC, the background temperature is calculated at three steps. Firstly, at each latitude
 174 band and pressure level, the daily zonal mean temperature (\bar{T}_d) is calculated by averaging the
 175 temperature profiles at ascending and the descending nodes, respectively. This largely removes the
 176 gravity waves, non-migrating tides, and long-period planetary waves. Here each latitude band has a
 177 width of 10° with centers offset by 5° from 80°S to 80°N . Secondly, linear regression is performed
 178 on \bar{T}_d at each node and is formulated as,

$$179 \quad \bar{T}_d = \bar{T}_{d0} + kt_{UT} + \bar{T}_{res}. \quad (1)$$

180 Here, \bar{T}_{d0} is the mean temperature in each YC. t_{UT} is the universal time with a unit of day, k
 181 represents the linear variation of \bar{T}_d in each YC. After removing \bar{T}_{d0} and the linear variation (kt_{UT})
 182 from \bar{T}_d , we get a residual temperature \bar{T}_{res} of each YC. Thirdly, tidal fitting is performed on \bar{T}_{res} of
 183 both nodes and is formulated as,

$$184 \quad \bar{T}_{res} = \bar{T}_{bk} + \sum_{n=1}^3 a_n \cos(n\omega t_{LT} - \varphi_n). \quad (2)$$

185 Here, $\omega = 2\pi/24$ is the rotation frequency of Earth with a unit of rad/hour, t_{LT} is the local time
 186 with a unit of hour, a_n and φ_n are, respectively, the amplitudes and phases of migrating diurnal
 187 ($n = 1$), semidiurnal ($n = 2$) and terdiurnal ($n = 3$). Now, \bar{T}_{bk} excludes atmospheric waves and is
 188 regarded as the mean temperature.

189 2.2 Removing seasonal variations from the mean temperature

190 Figure 1 shows that the center date of each YC shifts forward about one month from 2002 to
 191 2023. This forward drift induces the seasonal variation of temperature into \bar{T}_{bk} . This could further
 192 alias the long-term trend calculated from \bar{T}_{bk} and can be removed with the help of MSIS2.0. This is
 193 because MSIS2.0 has assimilated the SABER temperature profiles during 2002–2016. The
 194 climatological temperature of MSIS2.0 coincides with that of SABER within the uncertainties of \sim
 195 3 K in the MLT region (Emmert et al., 2021). The detailed procedure of removing seasonal
 196 variations is described below.

197 Firstly, we calculate the mean temperature of MSIS2.0. The temperature profiles (at 15
 198 longitudes and 24 LTs each day) are calculated from MSIS2.0 under the conditions of lower solar
 199 activity ($F_{10.7} = 50$ SFU) and geomagnetic quiet time ($ap = 4$ nT) throughout one calendar year.
 200 Such that solar and geomagnetic activities do not influence the seasonal variation and trend of the
 201 mean temperature. Then the daily zonal mean is performed on the temperature profiles of each day.

202 This removes tides and long-period planetary waves. The daily zonal mean temperature in each YC
 203 is averaged to get the mean temperature (\bar{T}_{MSIS}^{year} , the superscript means the YC in that year). Figures
 204 2(a1) and (a2) show the \bar{T}_{MSIS}^{year} at 70°N in YC3 and 70°S in YC6 during 2002–2023, respectively.

205 Secondly, we calculate the seasonal variations of each YC. The seasonal variations ($\Delta\bar{T}_{MSIS}^{year}$)
 206 caused by the forward drift of each YC in different years are quantified by the difference between
 207 \bar{T}_{MSIS}^{year} of that year and the reference year (i.e., \bar{T}_{MSIS}^{2002}). For example, the difference between 2003
 208 and 2002 is calculated as $\Delta\bar{T}_{MSIS}^{2003} = \bar{T}_{MSIS}^{2003} - \bar{T}_{MSIS}^{2002}$. More specifically, since \bar{T}_{MSIS}^{year} does not include
 209 the year-to-year variations of temperature but depends on the temporal span of YC only, $\Delta\bar{T}_{MSIS}^{2003}$ in
 210 YC3 represents the seasonal variation from 20th to 19th June. Figures 3(b1) and (b2) show $\Delta\bar{T}_{MSIS}^{year}$
 211 70°N in YC3 and 70°S in YC6 during 2002–2023, respectively. It is evident that the forward drift of
 212 YC induces temperature variations of ± 20 K at 70°N/S from 2002 to 2023, and should be removed
 213 before we determine the long-term trends in SABER temperature.

214

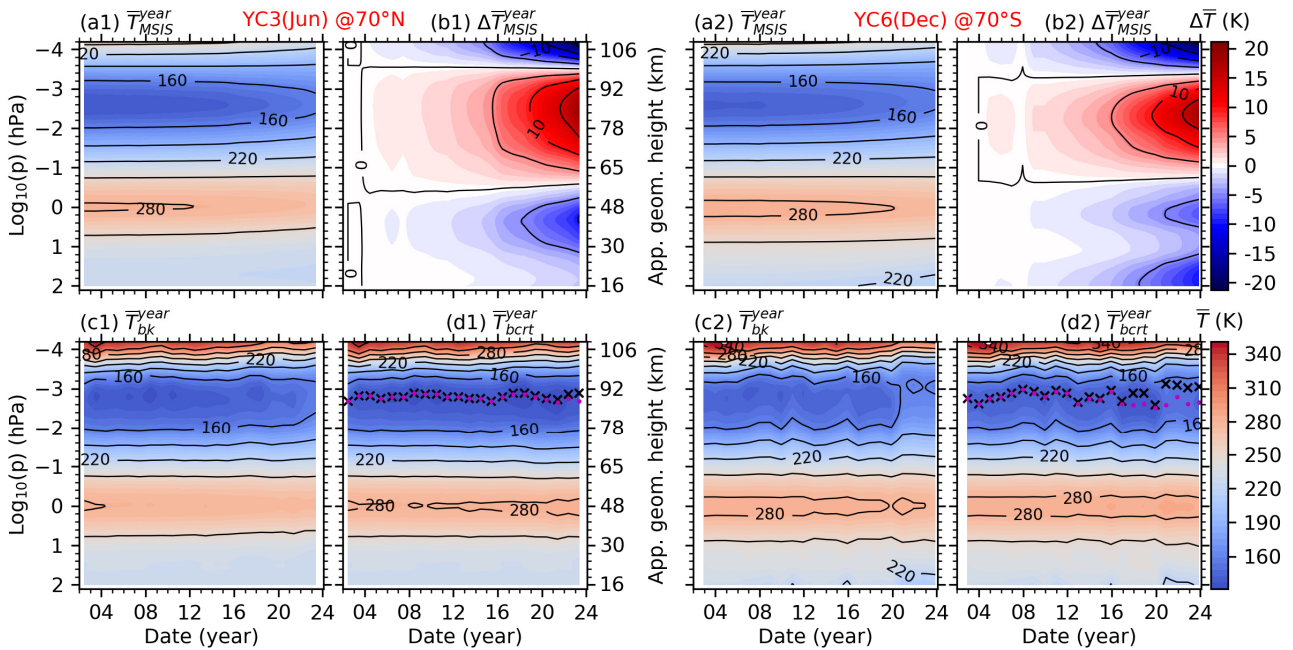


Figure 2. The date-height distributions of the mean temperature calculated from NRLMSIS 2.0 (\bar{T}_{MSIS}^{year}) and SABER (\bar{T}_{bk}^{year}) at 70°N in YC3 (left two columns) and 70°S in YC6 (right two columns). \bar{T}_{MSIS}^{year} is used as a reference to calculate the seasonal variation ($\Delta\bar{T}_{MSIS}^{year}$) caused by the forward drift of YC from 2002 to 2023. Then, the corrected mean temperature (\bar{T}_{bcr}^{year}) is calculated by removing $\Delta\bar{T}_{MSIS}^{year}$ from \bar{T}_{bk}^{year} . The mesopause altitudes calculated from \bar{T}_{bk}^{year} and \bar{T}_{bcr}^{year} are plotted as black cross and red dots, respectively. The plots of \bar{T}_{MSIS}^{year} , \bar{T}_{bk}^{year} , and \bar{T}_{bcr}^{year} have the same colorbar of \bar{T} . The plot of $\Delta\bar{T}_{MSIS}^{year}$ has the colorbar of $\Delta\bar{T}$. Same scales in y-axis are used in all panels. The approximate geometric height is label on the right of the second column.

215

216 Finally, we correct the mean temperature. The corrected mean temperature (\bar{T}_{bcrt}^{year} , shown in
 217 Figs. 3d1 and d2) is obtained by removing $\Delta\bar{T}_{MSIS}^{year}$ from \bar{T}_{bk}^{year} . This removes the seasonal variation
 218 caused by the forward drift of YC from 2002 to 2023. Moreover, \bar{T}_{bcrt}^{year} retains the long-term trend
 219 of the mean temperature. We note that, after removing $\Delta\bar{T}_{MSIS}^{year}$, \bar{T}_{bcrt}^{year} covered by each YC can be
 220 represented by its center date and half span in the reference year (Tab. 1). Table 1 also lists the
 221 approximate season related to each YC.

222
 223 **Table 1.** The date range of each YC and its corresponding season in the reference year of 2003

YCs	YC1	YC2	YC3	YC4	YC5	YC6
Date range	20/Feb±31	20/Apr±32	20/Jun±28	19/Aug±32	13/Oct±31	10/Dec±28
Season	later winter	later spring	summer	early autumn	later autumn	winter

225 2.3 Determining the long-term trend of the mean temperature

226 To calculate accurate trends in the MLT region, multi-year variations should be removed
 227 properly. The multi-year variations of temperature in the MLT region could be the solar cycle with a
 228 period of about 11 years (Beig et al., 2008; Tapping, 2013; Forbes et al., 2014; Gan et al., 2017;
 229 Qian et al., 2019), and the influences from below, such as the ~~stratospheric quasi-biennial oscillation~~
 230 ~~(QBO) with a period of about 28 months (Baldwin et al., 2001; Zhao et al., 2021) and~~ El Niño-
 231 Southern Oscillation (ENSO) with varying cycles of around 2–7 years (Domeisen et al., 2019; Li et
 232 al., 2013, 2016; Randel et al., 2009). The solar cycle can be represented by the solar radiation flux
 233 at 10.7 cm (i.e., $F_{10.7}$ with unit of SFU= $10^{-22}\text{Wm}^{-2}\text{Hz}^{-1}$) (Tapping, 2013). ENSO is represented by
 234 multivariate ENSO index (MEI) (Domeisen et al., 2019). ~~QBO is represented by the monthly mean~~
 235 ~~zonal wind measured by radiosonde at Singapore (Baldwin et al., 2001).~~ The multiple linear
 236 regression (MLR) method is effective to separate the long-term trend in temperature from the
 237 variations caused by solar cycle, ENSO and QBO. The MLR equation is formulated as,

$$238 Y(t) = c_0 + c_1 t + c_2 F_{10.7}(t) + c_3 \text{ENSO}(t) + c_4 \text{QBO}_{10}(t) + c_5 \text{QBO}_{30}(t) + \varepsilon(t). \quad (3)$$

240 Here, Y represents the mean temperature at year t from 2002 to 2023. c_0 represents a mean state of
 241 Y . c_1 is the long-term trend of Y . c_2, c_3, c_4, c_5 represent the contributions from solar cycle, ~~and~~
 242 ~~ENSO, and QBO zonal wind at 10 hPa (QBO₁₀) and 30 hPa (QBO₃₀), respectively.~~ The terms of
 243 $F_{10.7}$ ~~and~~, ENSO, ~~QBO₁₀, and QBO₃₀~~ are included in Eq. (3) for the purpose of determining long-
 244 term trend correctly but are not considered further in this work. Here we note that both the trends
 245 (linear variations) and quasi-periodical variations represent the natural variations in ~~QBO and~~
 246 ~~either the~~ predictors. These natural variations might influence the trends and variations of

247 temperature. Thus, MLR is applied to characterize the contributions from the natural variations of
248 predictors, and then the resulted trends of temperature exclude the trends inhibited in the predictors.
249 This is the trend studied in this work. Otherwise, if these predictors are de-trended, their residuals
250 are used in the MLR. The resulted trends of temperature may include the trends inhibited in
251 predictors.

252 The statistical significances of the regression coefficients are measured by the student-t test
253 and the variance-covariance matrix of Eq. (3). Specifically, in Eq. (3), the sampling points are 22,
254 and the predictor variables are 64. This results in the degree of freedom of 1619. Consequently, the
255 critical value is ~ 2.10 based on the student-t test at confidence level of 95% (Kutner et al., 2005).
256 This signifies that, with reference to the 95% confidence level, the magnitude of the regression
257 coefficient should be at least 2.1 times greater than the standard deviation.

258 2.4 Determining the mesopause of each yaw cycle

259 The mesopause temperature (\bar{T}_{msp}) is defined as the minimum of the mean temperature. The
260 pressure level where the minimum temperature occurs is defined as the mesopause altitude (z_{msp}).
261 Figures 2(d1) and (d2) show the mesopause altitudes calculated from \bar{T}_{bk}^{year} (black cross) and \bar{T}_{bcrt}^{year}
262 (red dot), respectively. We see that the mesopause altitudes calculated from \bar{T}_{bk}^{year} and \bar{T}_{bcrt}^{year} are
263 nearly identical in the first several years but exhibit discrepancies over the later several years. This
264 implies that the seasonal variation caused by the forward drift of YC affects the mesopause altitudes
265 to some extent. Moreover, the mesopause altitudes exhibit larger variabilities in the southern
266 summer polar region (YC6) than that in the northern summer polar region (YC3). Figure 3 shows
267 the date-latitude distributions of the mesopause temperature (\bar{T}_{msp}) and altitude (z_{msp}) calculated
268 from \bar{T}_{bcrt}^{year} . We note that z_{msp} is defined on pressure level initially (Fig. 2d). To compare with
269 previous studies, z_{msp} is interpolated onto the geometric heights in Fig. 3.

270 Previous SABER studies often discarded high latitudes possibly due to insufficient LT
271 coverage that induces uncertainties in the mean temperature estimation. A major advantage of
272 binning the SABER temperature based on YC is that an accurate mean temperature can be obtained.
273 Such that the latitude variations of \bar{T}_{msp} and z_{msp} at high latitudes can be thoroughly studied.
274 Firstly, we focus on the YCs in northern summer and winter (i.e., YC3 and YC6) because the
275 summer mesopause at high latitudes is more sensitive to the summer-to-winter circulation
276 (Dunkerton, 1978; Qian et al., 2017). In YC3 (YC6), \bar{T}_{msp} and z_{msp} decrease from 50°S to 80°N
277 (from 50°N to 80°S) in general. We note that \bar{T}_{msp} has local minima around the Equator throughout
278 the 22 years in YC3 and YC6 and is the coldest at the highest latitudes of the summer hemisphere.
279 z_{msp} is the lowest at 40–60°N/S throughout the 22 years. Besides the latitude variations, \bar{T}_{msp} and
280 z_{msp} also exhibit multi-year variations. For example, \bar{T}_{msp} is colder around the Equator during the

281 solar minima (i.e., 2007–2008, 2019–2021) in YC3 and YC6. In YC6, the lower z_{msp} at the
 282 southern higher latitudes might be related to the warm phase of ENSO during 2002–2005 and
 283 2016–2019.

284

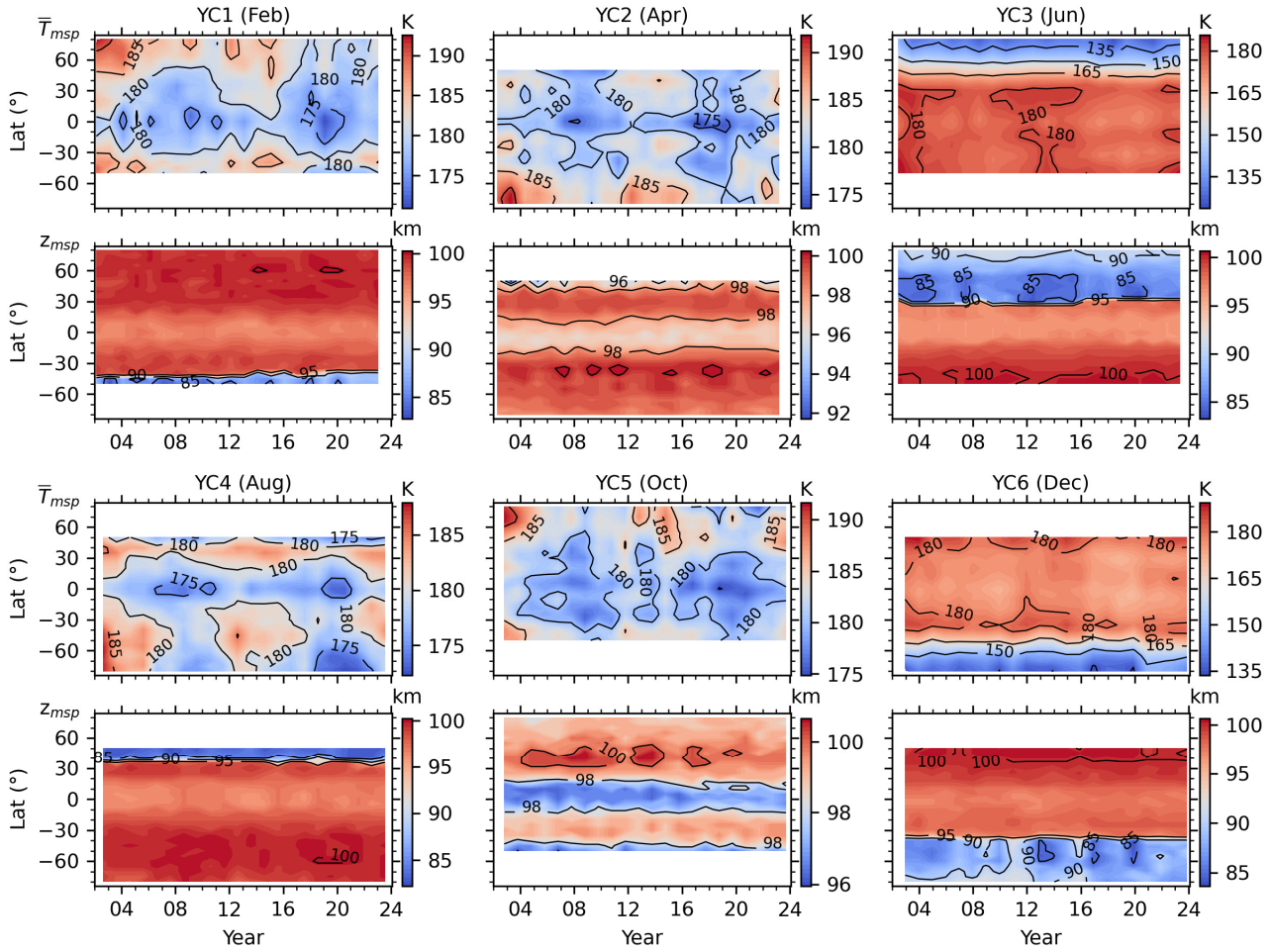


Figure 3. The date-latitude distributions of the mesopause temperature (\bar{T}_{msp} , the first and third rows) and altitude (z_{msp} , the second and fourth rows) calculated from \bar{T}_{bcrt}^{year} of each YC from 2002 to 2023. Here z_{msp} is interpolated from pressure level to geometric height.

285

286 In YC2 and YC5, the latitude variations of \bar{T}_{msp} and z_{msp} are almost hemispheric symmetry.
 287 \bar{T}_{msp} is the coldest around the Equator and the warmest at the highest latitudes. z_{msp} is the lowest at
 288 lower latitudes and the highest at the highest latitudes. In YC1, \bar{T}_{msp} and z_{msp} share the similar
 289 latitude variations in winter (YC6). The difference is that \bar{T}_{msp} is warmer in YC1 than that in YC6.
 290 z_{msp} is higher in YC1 than that in YC6. In YC4, \bar{T}_{msp} and z_{msp} share the similar latitude variations
 291 in summer (YC3). The difference is that \bar{T}_{msp} is warmer in YC4 than that in YC3. z_{msp} is higher in
 292 YC4 than that in YC3. In YC1–2 and YC4–5, multi-year variations of \bar{T}_{msp} exhibit clear solar cycle
 293 dependence. At lower latitudes, \bar{T}_{msp} are colder during the solar minima (i.e., 2006–2010, 2017–

294 2021). At high latitudes, \bar{T}_{msp} are warmer during the solar maxima (i.e., 2002–2005, 2012–2014,
 295 and after 2021). However, it looks like that the multi-year variations of z_{msp} are not as obvious as
 296 those of \bar{T}_{msp} . These multi-year variations are considered in Eq. (3) to separate the long-term trend
 297 in \bar{T}_{msp} correctly but are not considered further in this work.

298 3 Trends of temperature in the MLT region and mesopause

299 3.1 Trends of temperature in the MLT region

300 Trends of the corrected mean temperature and their significances of each YC are shown in Fig.
 301 4. These trends are generally larger at high latitudes than those at lower latitudes within the six YCs.
 302 Moreover, the trends show both hemispheric symmetry and asymmetry approximately in the high
 303 latitude MLT region.

304

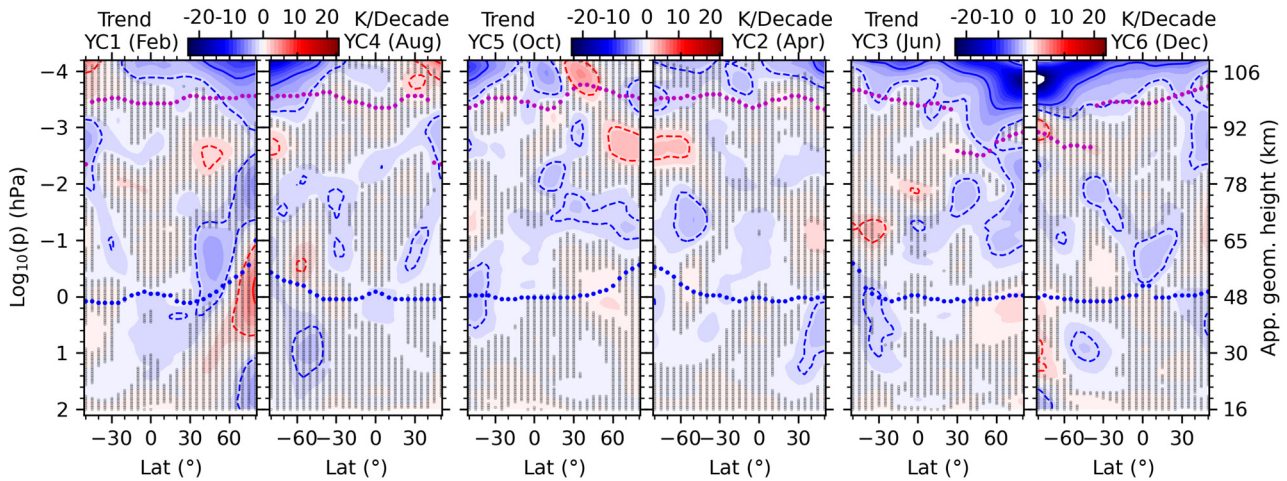


Figure 4. Trends of the corrected mean temperature in the six YCs. The solid and dashed contour lines indicate ± 6 and ± 2 K/decade, respectively. The purple and blue dots indicate the heights of the mesopause and stratopause, respectively. The regions marked by shaded points indicate that trends are not significant with reference to the 95% the confidence level. The approximate geometric height is label on the last panel.

305

306 First, we describe the hemispheric symmetry in the trends. In YC1 and YC4 and above 10^{-3}
 307 hPa, the cooling trends are ≥ 2 K/decade at latitudes higher than 40°N (YC1) and 40°S (YC4),
 308 respectively. Around 10^{-4} hPa, the cooling trends reach their peaks of ≥ 6 K/decade. In addition,
 309 there are also warming trends of ≥ 2 K/decade at latitudes higher than 30°S (YC1) and 30°N (YC4),
 310 respectively. Above mesopause, there are cooling trends of ≥ 2 K/decade observed within the latitude
 311 range of $20\text{--}50^\circ\text{S}$ for YC5 and $20\text{--}50^\circ\text{S}$ for YC2. Additionally, in the region just below 10^{-3} hPa,
 312 there are warming trends of ≥ 2 K/decade at latitudes of $50\text{--}80^\circ\text{N}$ for YC5 and $50\text{--}80^\circ\text{S}$ for YC2. In
 313 YC3 and YC6, the cooling trends of ≥ 2 K/decade shift upward from the mesopause at 80°N (YC3)

314 and 80°S (YC6) to 10⁻⁴ hPa at 50°S (YC3) and 50°N (YC6). There are also cooling trends of ≥6
315 K/decade at high latitudes of summer hemisphere. Meanwhile, the coldest trends are ≥10 K/decade
316 just below 10⁻⁴ hPa and at 80°N/S. Although the cooling trends in the MLT region have been
317 reported extensively at lower and middle latitudes (Beig et al., 2003; Laštovička, 2023), the extreme
318 cooling trends at high latitudes and above the summer mesopause have not been reported yet. We
319 note that the systematic error in the SABER operational processing is unknown. Its impacts on the
320 credibility of the trends derived here will be discussed in Sec.4.

321 Next, we describe the hemispheric asymmetry in the trends. In YC1 and YC4, the cooling
322 trends of ≥2 K/decade in YC1 extend to a wider latitude range (20°N–80°S) than those in YC4
323 (30°S–80°S) above 10⁻³ hPa. The insignificant warming trends of ≥2 K/decade can be seen in the
324 stratosphere at latitudes higher than 60°N in YC1 but at 45–60°S in YC4. In YC5 and YC2, the
325 cooling trends of ≥2 K/decade can be seen around the stratopause at 30–50°S (YC5) but below the
326 stratopause at 30–50°N (YC2). In YC3 and YC6, the significant warming trends of ≥2 K/decade in
327 YC6 are stronger than those in YC3 around 0.1 hPa. In addition, the warming trends near the
328 summer mesopause are significant in YC6 but insignificant in YC3. The simulation results in Qian
329 et al. (2019) also demonstrated warming trends in the southern summer MLT region. Specifically,
330 they showed significant warming trends below ~95 km and cooling trends above ~95 km at
331 latitudes exceeding 45°S between November and February. In contrast, there were insignificant or
332 warming trends at latitudes exceeding 45°N during June and July. Qian et al. (2019) attributed the
333 warming trend in the summer mesosphere to the changing meridional circulation.

334 **3.2 Structure and trends of the mesopause**

335 Taking advantages of the continuous measurements over a long-term (22 years or equivalently
336 two solar cycles), and YC binning at 50°S–80°N or 80°S–50°N, the robust mean states of the
337 mesopause temperature (\bar{T}_{msp}) and height (z_{msp}), as well as their trends and responses of \bar{T}_{msp} to
338 solar cycle, ENSO, QBO are quantified using MLR. Here we focus on the mean states and trends of
339 the mesopause temperature and altitude.

340 Figures 5(a) and 5(b) show the mean \bar{T}_{msp} and z_{msp} over 22 years of the six YCs. In YC1–2
341 and YC4–5, the mean \bar{T}_{msp} is in the range of 172–183 K but is warmer at latitudes higher than 40°N
342 (YC1) and 40°S (YC2) those in the counterparts of YC4 and YC5. The mean z_{msp} is mainly in the
343 range of ~96–102 km but is higher than ~85 km at 40–50°N (YC1) and 40–50°N (YC4). In YC3,
344 the mean \bar{T}_{msp} decreases sharply with latitudes from ~180 K at 30°N to ~125 K at 80°N. The mean
345 z_{msp} in YC3 reaches a minimum of ~85 km at 60°N. In YC6, the mean \bar{T}_{msp} decreases sharply with
346 latitudes from ~180 K at 35°S to ~135 K at 80°S. The mean z_{msp} in YC6 reaches a minimum of
347 ~86 km at ~50°S. The mean \bar{T}_{msp} (z_{msp}) in the northern summer polar region is colder (lower) than

348 that in the southern counterpart by $\sim 5\text{--}11\text{ K}$ ($\sim 1\text{ km}$). The hemispheric asymmetries of the summer
 349 mesopause temperature and altitude coincide with Xu et al. (2007), who used the SABER
 350 temperature data during 2002–2006 and showed that the mean \bar{T}_{msp} in the summer polar region of
 351 the NH is $\sim 5\text{--}10\text{ K}$ colder than its counterpart in the SH. A recent study by Wang et al. (2022), who
 352 used the SABER temperature data during 2002–2020, showed that the mean \bar{T}_{msp} in the summer
 353 polar region of the NH is $\sim 10\text{ K}$ colder than its counterpart in the SH. Moreover, the transition
 354 latitudes of the mean \bar{T}_{msp} (z_{msp}) from higher temperature (height) are 30°N in YC3 and 40°S in
 355 YC6. This coincides well with those reported by Xu et al. (2007) and Wang et al. (2022). These
 356 hemispheric asymmetries of the mean \bar{T}_{msp} and z_{msp} , and the transition latitudes could be caused
 357 by the hemispheric asymmetry of solar radiation and gravity wave forcing (Xu et al., 2007).
 358

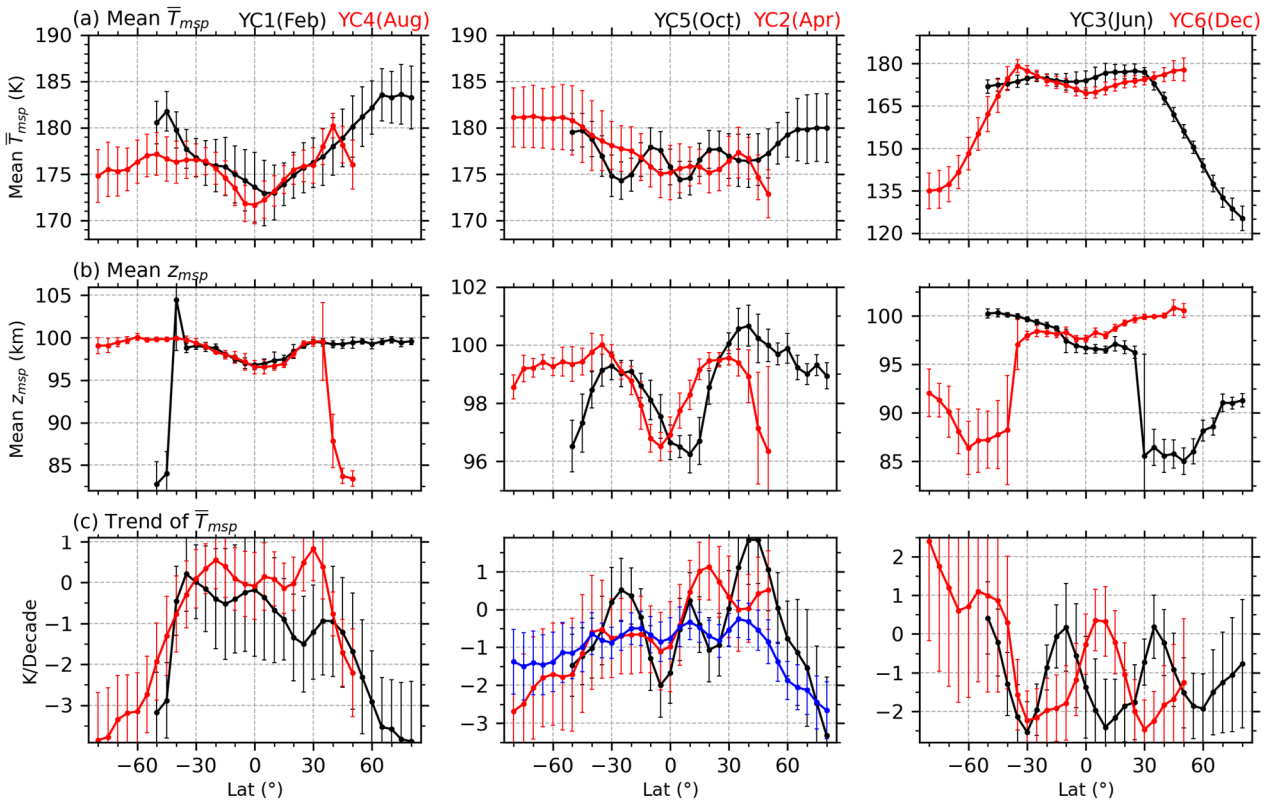


Figure 5. Latitude variations of the means of the mesopause temperature (\bar{T}_{msp} , a) and altitude (z_{msp} , b) and the trends of \bar{T}_{msp} (c) of the six YCs during 2002–2023. The error bar of each YC indicates 2.1 times standard deviation (i.e., at 95% confidence level according to the student-t test). The all-YC mean trend of mesopause temperature is shown as a blue line in the middle panel of (c).

359

360 Figure 5c shows that trends of \bar{T}_{msp} in YC1 and YC4 are extreme cooling ($\geq 2\text{ K/decade}$) at
 361 latitudes higher than 55°N/S . While at $40^\circ\text{S}\text{--}40^\circ\text{N}$, trends of \bar{T}_{msp} in YC1 are cooling with
 362 magnitudes of $\sim 0\text{--}2\text{ K/decade}$ but are warming in YC4 with magnitudes of $\sim 0\text{--}1\text{ K/decade}$. In YC2

363 and YC5, trends of \bar{T}_{msp} are either cooling or warming, depending on the specific latitudes and
364 months being considered. At southern latitudes, trends of \bar{T}_{msp} are cooling with magnitudes of ≥ 1
365 K/decade in YC2. Trends of \bar{T}_{msp} in YC5 change sharply from 2.0 K/decade at 45°N to -3
366 K/decade at 80°N. In YC3 and YC6, trends of \bar{T}_{msp} are mainly cooling except the insignificant
367 warming trends in YC6 and at latitudes higher than 40°S. Although trends of \bar{T}_{msp} are warming at
368 some latitudes of certain YC, the all-YC mean trends of \bar{T}_{msp} (blue line in Fig. 5c) are cooling with
369 magnitudes of 0.3–1 K/decade at 50°S–50°N. At latitudes higher than 55°S, the insignificant
370 cooling trends are ≤ 1.5 K/decade. In contrast, at latitudes higher than 55°N, the significant cooling
371 trends are ≥ 1.5 K/decade.

372 4 Discussions

373 The trends derived here may be influenced by the unknown systematic errors in the SABER
374 operational processing. The main causes of systematic errors are the lack of accurate knowledge of
375 the uncertainties in key parameters (mixing ratios of atomic oxygen (O) and carbon dioxide (CO₂))
376 and the nature of non-LTE (local thermodynamic equilibrium) in the SABER temperature retrieval.
377 The O mixing ratio provided to the SABER operational processing is from NRLMSISE-00 (Picone
378 et al., 2002). Below 100 km, no atmospheric observations of O are incorporated. Thus, the
379 uncertainty of O influences the uncertainties of temperature at ~75–110 km, in particular at 100–
380 110 km. The CO₂ mixing ratio provided to the SABER operational processing is the monthly
381 average value from WACCM model (Dawkins et al., 2018; Mlynczak et al., 2023). Thus, there is no
382 local time variation in CO₂ used in the operational SABER operational processing. The larger
383 vertical diffusion used in WACCM4 as compared to WACCM3 led to 15% uncertainty in CO₂ at
384 110 km. Mlynczak et al. (2023) showed that 15% uncertainty in CO₂ at 110 km an 8 K error in the
385 global mean (55°S–55°N) temperature. Moreover, the lack of correct trends and their coupling with
386 dynamical adjustments in O and CO₂ may also be sources of the systematic errors in SABER
387 temperature at high altitudes. At high altitudes and latitudes, non-LTE radiative transfer in CO₂
388 couple the vibrational temperatures at all altitudes due to the exchange of radiation among all
389 layers. Thus, any uncertainties in O or CO₂ at one layer will affect the temperature at all altitudes.
390 These uncertainties are systematic errors and cannot be reduced by averaging many profiles. Thus,
391 the trends derived here should be discussed rigorously based on the systematic errors of a single
392 temperature profile.

393 As reported at SABER web (<https://spdf.gsfc.nasa.gov/pub/data/timed/saber/>), one standard
394 deviation (corresponding to the confidence level of 68%) of the systematic error for a single
395 temperature profile is of ~1.4 K at and below 80 km, 4.0 K at 90 km, 5.0 K at 100 km, and 25.0 K
396 at 110 km for typical midlatitude condition. These errors may be larger at high latitudes. A rigorous

397 systematic error analysis is performed by assuming a negative systematic error (-E) in 2002 and a
398 positive systematic error (+E) in 2023. The difference of the two numbers over the 22 years is the
399 largest uncertainty caused by the systematic error (i.e., $2E/22 \approx 0.9E$ K/decade) and is named as
400 systematic trend uncertainty. Then, the number E is replaced by the systematic error reported at
401 SABER web. Such that one can get a systematic trend uncertainty for a given systematic error. We
402 note that the systematic trend uncertainty of $0.9E$ K/decade is the largest uncertainty caused by the
403 systematic error and is the worst case among all the combinations of systematic errors in different
404 years.

405 Based on the systematic error defined by one standard deviation at SABER web, the
406 systematic trend uncertainty during 2002–2023 caused by systematic errors at 110 km
407 ($\sim \log_{10}(6.3 \times 10^{-5} \text{ hPa}) = -4.2$) can be estimated as $50 \text{ K} / 22 \text{ years} \approx \pm 22.7 \text{ K/decade}$. In a same
408 manner, the systematic trend uncertainties are of 4.5 K/decade at 100 km ($\sim \log_{10}(2.8 \times 10^{-4} \text{ hPa}) = -$
409 3.6), 3.6 K/decade at 90 km ($\sim \log_{10}(1.4 \times 10^{-3} \text{ hPa}) = -2.9$), and 1.3 K/decade at and below 80 km
410 ($\sim \log_{10}(6.6 \times 10^{-3} \text{ hPa}) = -2.2$). We note that the systematic trend uncertainty will be doubled if the
411 systematic error is defined by two times of standard deviation (corresponding to the confidence
412 level of 95%). In the following discussions, we will compare the trends derived here with previous
413 observations and the systematic trend uncertainty calculated from the systematic error defined by
414 one standard deviation. If the derived trend is larger than the systematic trend uncertainty, the trend
415 is reliable. Otherwise, the trend is questionable.

416 The temporal interval of data may also influence the long-term trend (Laštovička and Jelínek,
417 ~~2019) Laštovička & Jelínek (2019) pointed out that the temporal interval of data might influence the~~
418 ~~long-term trend.~~ Using the nocturnal temperature in the MLT region measured by lidars around
419 41°N and 42°N over the period of 1990–2017, She et al. (2019) demonstrated that the cooling
420 trends are ~ 2.0 – 4.5 K/decade over only one solar cycle and are ~ 2.0 – 2.5 K/decade if the data
421 length is longer than two solar cycles. Using the SABER temperature profiles during 2002–2019,
422 Zhao et al. (2020) showed that the significant trends of \bar{T}_{msp} and their responses to solar cycle can
423 be obtained at 50°S – 50°N over longer than one solar cycle. Both She et al. (2019) and Zhao et al.
424 (2020) showed that the trends are relatively insensitive to the specific beginning and ending time of
425 the data as compared to the data length. Since the data length used in this study spans approximately
426 two solar cycles, the derived trends are highly reliable in statistical sense. In the following
427 discussions, the reliability of trends will also be determined by comparing them with the systematic
428 trend uncertainty.

429 **4.1 The reliability of trends in the MLT region at latitudes lower than 50°N/S**

430 To facilitate a comparison with previously reported the annual and global-mean trends in the
431 MLT region, we present the mean trends of the corrected mean temperature at 50°S – 50°N and at

432 55–80°S or 55–80°N of the six YCs (Fig. 6). The mean trends at 50°S–50°N of each YC are cooling
433 with magnitudes of ~ 0.5 – 1 K/decade at 10 – 10^3 hPa. The exception is the warming trend of 0.2
434 K/decade around 10^2 hPa in YC1 and of 0.1 K/decade around 4×10^3 hPa in YC3. Above 5×10^3
435 hPa, the cooling trends increase sharply with altitude and reach to ~ 2 K/decade in YC5 and to ~ 3
436 K/decade in YC2 at 10^4 hPa. Compared to the situation in YC2 and YC5, the cooling trends
437 increase more sharply with altitude in YC3 and YC6. Their magnitudes change nearly identically
438 and are from ~ 0.5 K/decade at 2×10^3 hPa to ≥ 5 K/decade at 10^4 hPa. When the mean trends at
439 50°S–50°N across all-YC are further averaged, we obtain an annual mean trend (blue line in Fig.
440 6a). The annual mean trend is cooling with magnitudes of ~ 0.5 – 0.8 K/decade and vary with altitude
441 slightly at 10 – 5×10^4 hPa.

442 The altitude variation and the magnitude of the annual mean trend are similar to the previous
443 results (Garcia et al., 2019; Mlynchak et al., 2022; Zhao et al., 2021). Figure 3 of Garcia et al.
444 (2019) revealed that the global mean (52°S–52°N) SABER temperature trends are cooling with
445 magnitudes of ~ 0.5 – 0.9 K/decade at 10 – 5×10^4 hPa during 2002–2018. These magnitudes are
446 slightly smaller than those derived from WACCM. Table 1 of Mlynchak et al. (2022) demonstrated
447 that the global mean (55°S–55°N) SABER temperature also display cooling trends with magnitudes
448 of ~ 0.51 – 0.63 K/decade at 1 – 10^3 hPa. Similarly, Fig. 4 of Zhao et al. (2021) revealed that the
449 global mean (50°S–50°N) SABER temperature trends are cooling with magnitudes of ~ 0.5 – 0.9
450 K/decade at 30–105 km. At 10^4 hPa, the extreme cooling trend of 2.6 K/decade in Table 1 of
451 Mlynchak et al. (2022) is slightly smaller than the 2.8 K/decade derived here but within 2 times of
452 the standard deviation (blue line in Fig. 6a). Further examining the trends across the six YCs (Figs.
453 4 and 6a), it becomes evident that the extreme cooling trend is mainly attributed to the middle
454 latitudes of summer hemisphere (i.e., YC3 and YC6) and partially from other months. As suggested
455 by Mlynchak et al. (2022), the extreme cooling trend at 10^4 hPa is due to a decrease in solar
456 irradiance that is not captured by the $F_{10.7}$ index.

457 We note that these trends are derived from the SABER temperature. The systematic error of
458 SABER temperature influences the credibility of these derived trends. According to the rigorous
459 analysis of the systematic error, the trends derived here are reliable only if their magnitudes are
460 larger than the systematic trend uncertainty. The annual and global-mean trends are cooling with
461 magnitudes of 2–4 K/decade around 10^4 hPa are unreliable. Because these values are in the range
462 of the systematic trend uncertainty of 22.7 K/decade at 6.3×10^5 hPa and 4.5 K/decade at 2.8×10^4
463 hPa. At pressure levels lower than 10^3 hPa, the annual and global-mean trends are cooling with
464 magnitudes of ~ 0.5 – 1 K/decade are unreliable. Because these values are in the range of the
465 systematic trend uncertainty of 3.6 K/decade around 10^3 hPa and 1.3 K/decade below 6.6×10^3 hPa.

466 These detailed comparisons showed that the trends at pressure levels reported by Garcia et al.

467 (2019) and Mlynczak et al. (2022) support the altitude variations and magnitudes of the trends
 468 derived here directly. Although the trends reported by Zhao et al. (2021) are in geometric height,
 469 their altitude variations and magnitudes agree with the trends derived here, too. Thus, the method of
 470 binning SABER samplings based on YC leads a reliable global mean trends at 50°S–50°N However,
 471 these trends are unreliable since their magnitudes are in the range of the systematic trend
 472 uncertainties. Moreover, We note that –the method of binning SABER samplings based on YC
 473 this method provides an opportunity to study the trends at latitudes higher than 50°N/S in certain
 474 months.

475

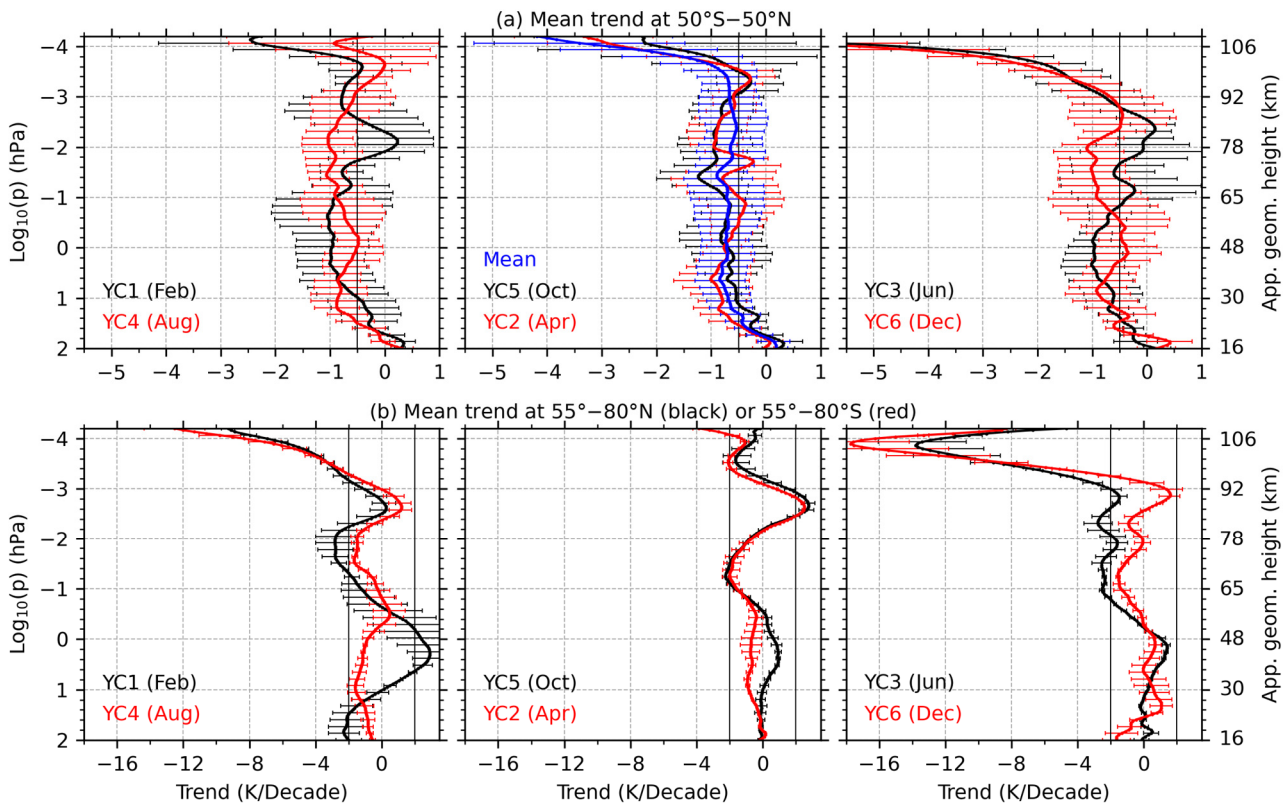


Figure 6. Mean trends of the corrected mean temperature at 50°S–50°N (a) and at 55–80°S (red line in b) or 55–80°N (black line in b) of the six YCs. The annual mean trend is calculated by averaging the trends of the six YCs at 50°S–50°N and is shown a blue line in the middle panel of (a). The error bars indicate standard errors of the averaged data.

476

477 4.2 The reliability of trends in the MLT region at latitudes higher than 50°N/S

478 At latitudes higher than 50°N/S, the altitude variations of the mean trends of the six YCs (Fig.
 479 6b) are seasonal symmetric approximately above 1 hPa. The magnitudes of trends are mainly in the
 480 range of -2–2 K/decade below the height of 10^{-3} hPa. These trends are larger than the systematic
 481 trend uncertainties of 1.3 K/decade and thus are reliable below 6.6×10^{-3} hPa. However, these trends
 482 are in the range of the systematic trend uncertainties of 3.6 K/decade and thus are unreliable around

483 10⁻³ hPa. An interesting feature is the warming trends of 1–2.5 K/decade at 10⁻²–10⁻³ hPa in April,
 484 August, October, and December. The altitudes of peaks of the warming trends vary from 4×10⁻³ hPa
 485 to 10⁻³ hPa in different months. Focusing on the latitude band of 64–70°N in June and 64–70°S in
 486 December, Bailey et al. (2021) merged the temperature data from HALO and SABER (total length
 487 of 29 years) and HALOE and SOFIE (total length of 22 years). Their analysis revealed warming
 488 trends of 1–2 K/decade near 5×10⁻³ hPa (~85 km) at 64–70°N in June and 64–70°S in December, as
 489 illustrated in Fig. 7 of their paper. The results simulated by WACCM-X showed significant warming
 490 trends at ~80–95 km at latitudes higher than 45°S from November to February and close to zero or
 491 warming trends at latitudes higher than 45°N from June to July (Qian et al., 2019). The warming
 492 trends in December derived here coincides with those reported by Bailey et al. (2021) and Qian et
 493 al. (2019). The weak warming trend at 2×10⁻³ hPa in June coincides with those in Qian et al. (2021)
 494 but is much smaller than the 1–2 K/decade reported by Bailey et al. (2021). In April and October,
 495 the warming trends are hemispheric symmetric at 10⁻²–10⁻³ hPa and reach peak of ≥2 K/decade at
 496 3×10⁻³ hPa. It should be noted that, the warming trends of 1–2.5 K/decade at 10⁻²–10⁻³ hPa are in
 497 the range of the systematic trend uncertainties of 1.3 K/decade at 6.6×10⁻³ hPa and of 3.6 K/decade
 498 around 10⁻³ hPa. Thus they are unreliable in the sense of systematic trend uncertainty. Above 10⁻³
 499 hPa, the trends transit from warming to cooling.

500 We can see the extreme cooling trends of ≥6 K/decade above ~10⁻³ hPa and in YC3 and YC6
 501 also in YC1 and YC4 but around 10⁻⁴ hPa. Due to the systematic trend uncertainty, these trends are
 502 reliable around 10⁻³ hPa but unreliable around 10⁻⁴ hPa. These cooling trends are comparable with
 503 the global average mesosphere temperature of 6.8–8.4 K/decade derived by Mlynczak et al. (2022)
 504 after doubling of CO₂ at Earth's surface in the MLT region. However, it takes decades to doubled
 505 CO₂. Thus, a purely radiative effect due to the increasing CO₂ cannot support the extrem cooling
 506 trends derived here. Mlynczak et al. (2022) proposed that the F10.7 is not a suitable proxy to
 507 indicate effects of the solar radiations on the lower thermosphere. But the solar irradiance in the
 508 Schumann–Runge band (175–200 nm) might be responsible for the colder trend. Even so, the
 509 extreme cooling trends of ~10 K/decade are still larger than those reported by Mlynczak et al.
 510 (2022). Other possible reasons for the extreme cooling trends in the high latitude MLT region can
 511 be attributed to: ~~(1) the dynamical feedback in the polar MLT region;~~ ~~(2) the uncertainties of the~~
 512 SABER temperature measurements.

513 Besides the purely radiative effect on the cooling trends in the MLT region (i.e., Garcia et al.,
 514 2019, Mlynczak et al., 2022), the dynamical feedback might be another cause of the cooling trends.
 515 Based on the simplified transformed Eulerian mean (TEM) thermodynamic equation, the
 516 temperature change (ΔT) caused by dynamics can be written as (Eq. 3 and 4 of Yu et al. (2023)),

$$\Delta T = -\alpha^{-1} \left(w^* S + v^* \frac{\partial \bar{T}}{\partial \varphi} \right). \quad (4)$$

518 Here, α is the Newtonian cooling coefficient. w^* and v^* are the residual vertical and meridional
519 velocity, respectively. S and \bar{T} are the static stability and zonal mean temperature, respectively. a
520 and φ are the Earth's radius and latitude, respectively. From Eq. (4), we propose that the extreme
521 cooling trends at high latitudes of the summer hemispheres (YC3 and YC6) might be resulted from
522 the changing summer-to-winter circulation and gravity wave forcing in the MLT region. The
523 circulation is upwelling (positive w^*) in the summer hemisphere and causes a cold summer
524 mesosphere through adiabatic cooling. Conversely, in the winter hemisphere, the circulation is
525 downwelling (negative w^*), leading to a warm winter mesosphere through adiabatic warming
526 (Garcia and Solomon, 1985). A necessary condition for the extreme cooling trends at summer high
527 latitudes is the stronger upwelling and thus the increasing gravity wave body force in the summer
528 hemispheres. Previous studies showed that the potential energy of gravity waves (GWPE) in the
529 MLT region exhibited significant positive trends at southern high latitudes in January and at
530 northern high latitudes in July (Fig. 5 of Liu et al., 2017). The positive trends of GWPE might
531 enhance the strength of upwelling and thus result in the extreme cooling trends at high latitudes of
532 summer hemispheres. It should be noted that the dynamical feedback in the MLT region is only
533 analyzed qualitatively, the quantitative analysis should be performed through model simulations.
534 Such that one can elucidate the physics behind the strong cooling trend in the polar MLT region.

~~535 The main causes of the operational SABER temperature systematic uncertainties are the lack
536 of accurate knowledge of atomic oxygen and carbon dioxide during the retrieval process. The
537 atomic oxygen provided to the operational SABER temperature retrieval algorithm is from
538 NRLMSISE-00 (Picone et al., 2002). Below 100 km, no atmospheric observations of atomic
539 oxygen are incorporated. Thus, the uncertainty of atomic oxygen influences the uncertainties of
540 temperature from ~75 km to 110 km, in particular, above 100 km. The carbon dioxide provided to
541 the operational SABER temperature retrieval algorithm is the monthly average value from WACCM
542 model (Dawkins et al., 2018; Picone et al., 2002). Thus, there is no local time variation in carbon
543 dioxide used in the operational SABER temperature algorithm. This will induce uncertainties of
544 SABER temperature and thus the uncertainties of trends above 75 km.~~

~~545 These uncertainties in temperature may not be constant or stable in time or in space. To explore
546 the impacts of the uncertainties in SABER temperature on the derived trends, we performed Monte
547 Carlo simulations by assuming the uncertainties in SABER temperature following a uniform
548 distribution in the range of $\pm 25\text{K}$. In each time of Monte Carlo simulation, in each YC and at each
549 pressure level and within a latitude band of 10° , the SABER samplings (more than 5000 data) are
550 added by random numbers following the uniform distribution in the range of $\pm 25\text{K}$. Then same
551 procedure described in Sec. 2.1-2.3 was repeated to derive trends. The Monte Carlo simulations
552 were performed 5000 times (see Appendix). The main result is that the uncertainties of $\pm 25\text{K}$ in~~

553 ~~SABER samplings would induce a mean temperature variation of $\sim 1-3$ K and a false trend of $\sim 0.5-$
554 1.2 K/decade at high latitudes. This is mainly because the mean temperature is calculated from
555 more than 5000 data in each YC within a latitude band of 10° , which reduces the standard deviation
556 by a factor of $\sim 1/250$ based on central limit theory. It must be noted that the actual distributions of
557 the uncertainties in SABER samplings caused by atomic oxygen and carbon dioxide are unknown.
558 The Monte Carlo simulation only provides a reference result by assuming the uncertainties
559 following uniform distributions. This may not be valid for the case of SABER temperature
560 systematic errors. So may not be valid. We only include it in the Appendix.~~

561 4.3 The reliability of the mesopause trends

562 The trends of \bar{T}_{msp} derived in this study are significant and mainly negative at $50^\circ\text{S}-50^\circ\text{N}$
563 across most YCs. The averaged trend of \bar{T}_{msp} of the six YCs is -0.64 ± 0.22 K/decade over $50^\circ\text{S}-$
564 50°N . When the average is performed over $80^\circ\text{S}-80^\circ\text{N}$, the trend of \bar{T}_{msp} of the six YCs is $-$
565 1.03 ± 0.40 K/decade. The cooling trend of \bar{T}_{msp} derived here coincides also with the -0.5 ± 0.21
566 K/decade in the mesosphere (Garcia et al., 2019) within only $50^\circ\text{S}-50^\circ\text{N}$. Compared to the trend
567 derived from sodium lidar observations during nighttime only around 40°N , the trends of \bar{T}_{msp} from
568 SABER are about $-0.1, 0.0, -0.2, -0.8, 0.6, -1.9$ K/decade in the six YCs and have annual mean of $-$
569 0.4 K/decade. This is less than the significant cooling trend of $2.3-2.5$ K/decade during 1990–2018
570 but is consistent with the insignificant cooling trend of $0.2-1$ K/decade during 2000–2018 (Yuan et
571 al., 2019). The comparisons of \bar{T}_{msp} between our results and those from satellite, ground-based
572 observations exhibit general consistencies in the sense of annual mean or global-mean. However,
573 the z_{msp} is mainly above 95 km (6.5×10^{-4} hPa), where the systematic trend uncertainties are larger
574 than 3.8 K/decade and are larger than the trends of \bar{T}_{msp} . Thus, the trends of \bar{T}_{msp} derived here are
575 mainly unreliable in the sense of rigorous systematic error analysis.

576 A notable feature is the warming trends of \bar{T}_{msp} with magnitudes of $0-2$ K/decade at latitudes
577 higher than 40°S in YC6. This warming trend is insignificant under 95% confidence level. If we
578 change the temporal interval from 2002–2023 to 2002–2019, the trends of \bar{T}_{msp} are cooling with
579 magnitudes of $1-2$ K/decade. Here we note that the year 2020 is just after the time when the
580 SABER temperature data was revised (version 2.08, since 15 December 2019) (Mlynczak et al.,
581 2023). In this work, we use the SABER temperature data of versions 2.07 (before 15 December
582 2019) and 2.08 (after 15 December 2019). According to Mlynczak et al. (2023), the new released
583 data are free from the algorithm instability. On the other hand, there is no significant difference in
584 the counterpart of YC3. A recent study by Yu et al. (2023) showed that the Hunga Tonga Hunga-
585 Ha'apai (HTHH) volcanic eruption on 15 January 2022 induced temperature anomalies of ± 10 K
586 globally in the stratosphere and mesosphere in August. The anomalies disappeared after September

587 2022. This indicates that the volcanic eruption may influence the mesosphere temperature through
588 circulations and waves. From the mesopause temperature of YC6 shown in Fig. 3, we see that the
589 warmer mesopause occurred after 2020 before the HTHH volcanic eruption. Thus, the largest
590 difference in YC6 may not be caused by the algorithm instability or the HTHH volcanic eruption but
591 a realistic result. As shown in Figs. 2(d) and 5(b) and reported by Wang et al. (2022), the annual
592 variability of z_{msp} is ~ 5 km at the southern high latitudes (YC6) but is relative stable at the northern
593 high latitudes (YC3). The large annual variability of z_{msp} induces a large variability of \bar{T}_{msp}
594 (indicated by large standard deviations in the right panel of Fig. 5b). This in turn contributes to the
595 large variability of the trends of \bar{T}_{msp} at southern high latitudes. Another possible reason is that the
596 warming trends of 0–2 K/decade are unreliable due to the large systematic trend uncertainties in this
597 height range.

598 5 Summary

599 Using the temperature profiles measured by the SABER instrument throughout the period of
600 2002–2023 (about two solar cycles) and binning them based on yaw cycles (YCs), we get
601 continuous data with good LT coverage within the range of 50°S–80°N or 80°S–50°N. Then we can
602 obtain an accurate mean temperature excluding atmospheric waves. The temporal span of each YC
603 drifted forward about one month from 2002 to 2023, aliasing the seasonal change in temperature
604 into long-term trends. This season change is removed by using the climatological temperature of
605 MSISE2.0. The remaining temperature is regarded as the corrected mean temperature (\bar{T}_{bcrt}^{year}) of
606 each YC. Then the mesopause temperature (\bar{T}_{msp}) and height (\bar{z}_{msp}) are calculated from \bar{T}_{bcrt}^{year} .
607 Such that the trends of the mean temperature and the mesopause structure can be studied in each YC
608 at high latitudes using MLR. The main results are summarized as below:

609 The cooling trends are significant in the MLT region and coincide well with previous results at
610 50°S–50°N. At latitudes higher than 55°N, the new findings are that the cooling trends have
611 magnitudes of ≥ 2 K/decade at northern high latitudes in February, April, and June and at southern
612 high latitudes in August, October, and December. There are also extreme cooling trends of ≥ 6
613 K/decade in the lower thermosphere at the northern high latitude in February and June and at the
614 southern high latitudes in August and December. Both the cooling and extreme cooling trends are
615 hemispheric and seasonal symmetric. It should be noted that the annual and global-mean trends are
616 unreliable in the sense of rigorous systematic error analysis. The trend of each YC are are reliable
617 only below 6.6×10^{-3} hPa. The extreme cooling trends of ≥ 6 K/decade in YC3 and YC6 are reliable
618 above $\sim 10^{-3}$ hPa in the sense of rigorous systematic error analysis.

619 Besides the general cooling trends, there are also warming trends of 1–2.5 K/decade at 10^2 – 10^3
620 hPa and at latitudes higher than 55°N in October and December and at latitudes higher than 55°S

621 in April and August. The peaks of the warming trends vary from 4×10^{-3} hPa to 10^{-3} hPa in different
622 months. The warming trend in December coincides with previous observational and simulation
623 results. However, these warming trends are in the range of the systematic trend uncertainties.

624 The mean $\bar{T}_{msp}(z_{msp})$ in the northern summer polar region is colder (lower) than that in the
625 southern counterpart by a value of $\sim 5\text{--}11$ K (~ 1 km) over the past 22 years. Although the trends of
626 \bar{T}_{msp} are highly dependent on latitudes and months, they are negative at most latitudes and have
627 larger magnitudes at higher latitudes. The trends of \bar{T}_{msp} at the southern high latitudes in December
628 are highly dependent on the data length. The trends of \bar{T}_{msp} change from warming of $0\text{--}2$ K/decade
629 during 2002–2023 to cooling of $1\text{--}2$ K/decade during 2002–2019. The significant dependence of the
630 trends of \bar{T}_{msp} on the data length might be caused by the large annual variability of z_{msp} at the
631 southern high latitudes in December. However, the trends of \bar{T}_{msp} derived here are mainly
632 unreliable in the sense of rigorous systematic analysis.

633 The trends of the mean temperature in the MLT region and mesopause are revealed from
634 continuous observations of the SABER instrument over the past 22 years. The data length is long
635 enough to determine reliable trends. Our results provide an observational proof that the extreme
636 cooling trends at high latitudes are more sensitive to the changing dynamics associated with climate
637 change and should be paid more attentions in future observational and model studies. Another
638 important issue is the systematic error in SABER operational processing. The trends derived here
639 are mostly unreliable in the sense of rigorous systematic error analysis. The only reliable trends are
640 the extreme cooling trends of ≥ 6 K/decade in YC3 and YC6.

641 **Appendix**

642 ~~Around 10^{-4} hPa, the uncertainties of SABER temperature measurements are around 25 K at~~
643 ~~mid-latitudes and are likely higher at high latitudes. These uncertainties are mainly attributed to the~~
644 ~~uncertainties of atomic oxygen and carbon dioxide, which were used in the operational SABER~~
645 ~~temperature retrieval algorithm. Moreover, these uncertainties in temperature may not be constant~~
646 ~~or stable in time or in space. To explore the impacts of the uncertainties in SABER temperature on~~
647 ~~the derived trends, we performed Monte Carlo simulations by assuming the uncertainties in SABER~~
648 ~~temperature following a uniform distribution in the range of ± 25 K. In each time of Monte Carlo~~
649 ~~simulation, in each YC and at each pressure level and within a latitude band of 10° , the SABER~~
650 ~~samplings (more than 5000 data) are added by random numbers following the uniform distribution~~
651 ~~in the range of ± 25 K. Then same procedure described in Sec. 2.1–2.3 was repeated to derive trends.~~
652 ~~The Monte Carlo simulations were performed 5000 times to get convincing results.~~

653 ~~Since the cooling trends are very large in YC3 and at 75° N, especially around the pressure~~
654 ~~levels of around 10^{-4} hPa, we show in Figure A the impact of the random uncertainties of SABER~~

655 temperature on the derived trends in YC3 and at 75°N. The uncertainties of ± 25 K in SABER
 656 samplings induce the mean temperature (\bar{T}_{bk}^{2002}) varying in the range of ± 2 K (Fig. Aa1) with
 657 standard deviation of 0.5 K (Fig. Aa2) at 10^{-4} hPa. This in turn induces the trends varying in the
 658 range of ± 0.6 K/decade (Fig. Ab1) with standard deviation of 0.15 K/decade (Fig. Ab2) at 10^{-4} hPa.
 659 The altitude profile of \bar{T}_{bk}^{2002} by assuming a zero uncertainty is similar to that calculated by
 660 assuming the random uncertainties of ± 25 K (Fig. Ac1). The differences of the maximum and
 661 minimum of \bar{T}_{bk}^{2002} among the 5000 times of Monte Carlo simulations are ~ 1.2 K below 5×10^{-4} hPa
 662 and are ≥ 3 K around 10^{-4} hPa (Fig. Ac2). The altitude profile of trend by assuming a zero
 663 uncertainty is similar to that calculated by assuming the random uncertainties of ± 25 K (Fig. Ad1).
 664 The differences of the maximum and minimum of trend among the 5000 times of Monte Carlo
 665 simulations are ~ 0.5 K/decade below 10^{-3} hPa and are ~ 0.5 – 1.2 K/decade around 10^{-4} hPa (Fig.
 666 Ad2). This example illustrates that the uncertainties of ± 25 K in SABER samplings would induce a
 667 mean temperature variation of ~ 1 – 3 K and a false trend of ~ 0.5 – 1.2 K/decade at high latitudes.

668

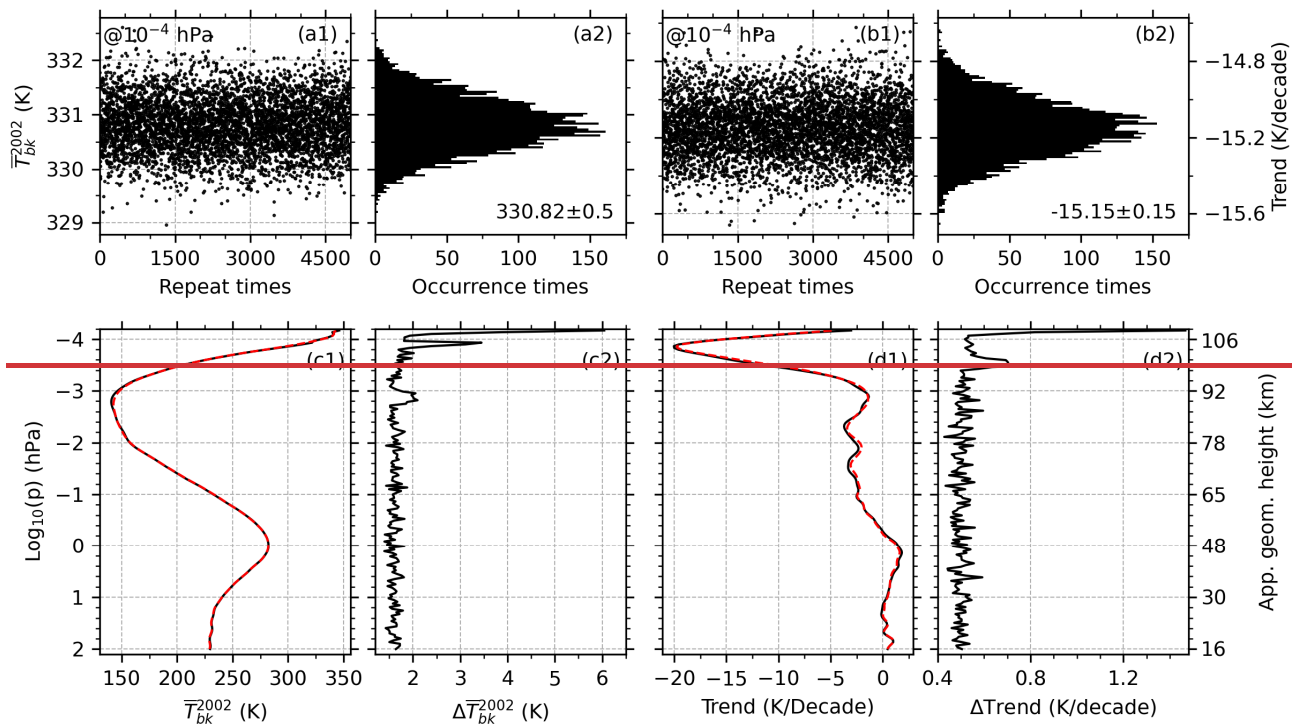


Figure A. The impacts of random uncertainties of ± 25 K in SABER temperature on the derived trends in YC3 and at 75°N during 5000 times of Monte Carlo simulation. (a1) and (a2): the mean temperature calculated from SABER sampling (\bar{T}_{bk}^{2002}) and its histogram at 10^{-4} hPa; (b1) and (b2): the trend and its histogram at 10^{-4} hPa; (c1) and (d1): the altitude profiles of \bar{T}_{bk}^{2002} by assuming zero uncertainty (black) and random uncertainties of ± 25 K (dashed black); (c2) and (d2) altitude profile of the difference between the maximum and minimum of \bar{T}_{bk}^{2002} and trend.

669

670 ~~Another Monte Carlo simulation is performed to test the impacts of the uncertainties of $\pm 25\text{K}$~~
671 ~~on the mean temperature (180 K) by changing the sampling points. During 5000 times of~~
672 ~~simulations (not shown here), the mean temperature and its standard deviation are 179.956 ± 4.5 K if~~
673 ~~there are 10 samplings; the mean temperature and its standard deviation are 179.977 ± 1.43 K if there~~
674 ~~are 100 samplings; the mean temperature and its standard deviation are 179.997 ± 0.20 K if there are~~
675 ~~5000 samplings. This indicates that the increasing samplings can reduce the measurement~~
676 ~~uncertainties efficiently. Although the uncertainties of SABER samplings are as large as $\pm 25\text{K}$ at~~
677 ~~high latitudes, its impact on the trends are insignificant in the highly averaged results. This is mainly~~
678 ~~because mean temperature is calculated from more than 5000 data in each YC within a latitude band~~
679 ~~of 10° , which reduces the standard deviation by a factor of $\sim 1/250$ based on central limit theory. It~~
680 ~~must be noted that the actual distributions of the uncertainties in SABER samplings are unknown.~~
681 ~~The Monte Carlo simulation only provides a reference result by assuming the uncertainties~~
682 ~~following uniform distribution. This may not be valid for the case of SABER temperature~~
683 ~~systematic errors.~~

684

685 **Author contributions**

686 XL analyzed the data and prepared the paper with assistance from all co-authors. JX and JY
687 design the study. All authors reviewed and commented on the paper.

688 **Data Availability Statement**

689 All SABER data can be accessed from Space Physics Data Facility, Goddard Space Flight
690 Center (<https://spdf.gsfc.nasa.gov/pub/data/timed/saber/> (last access: January 2024; Mlynczak et al.,
691 2023). The $F_{10.7}$ data were obtained from <https://spdf.gsfc.nasa.gov/pub/data/omni/> (last access:
692 January 2024; Tapping, 2013). ~~The QBO data were obtained from [https://acd-](https://acd-ext.gsfc.nasa.gov/Data_services/met/qbo/)~~
693 ~~ext.gsfc.nasa.gov/Data_services/met/qbo/ (last access: January 2024; Baldwin et al., 2001).~~ The
694 ENSO data were obtained from <https://www.psl.noaa.gov/enso/mei/> (last access: January 2024;
695 Zhang et al., 2019; Wolter and Timlin, 2011)

696 **Competing interests**

697 The authors declare that they have no conflict of interest.

698 **Acknowledgments**

699 This work was supported by the National Natural Science Foundation of China (41874182,
700 42174196), the Project of Stable Support for Youth Team in Basic Research Field, CAS (YSBR-
701 018), the Informatization Plan of Chinese Academy of Sciences (CAS-WX2021PY-0101), and the

702 Open Research Project of Large Research Infrastructures of CAS "Study on the interaction between
703 low/mid-latitude atmosphere and ionosphere based on the Chinese Meridian Project". This work
704 was also supported in part by the Specialized Research Fund and the Open Research Program of the
705 State Key Laboratory of Space Weather. We are very grateful for the helpful comments by Jan
706 Laštovička, Martin Mlynczak, [Tao Yuan](#), and [Ana G. Elias](#)~~one anonymous reviewer~~.

707 **References**

- 708 Bailey, S. M., Thuraiajah, B., Hervig, M. E., Siskind, D. E., Russell, J. M., and Gordley, L. L.: Trends in the polar
709 summer mesosphere temperature and pressure altitude from satellite observations, *J. Atmos. Solar-Terrestrial*
710 *Phys.*, 220, 105650, <https://doi.org/10.1016/j.jastp.2021.105650>, 2021.
- 711 Beig, G., Keckhut, P., Lowe, R. P., Roble, R. G., Mlynczak, M. G., Scheer, J., Fomichev, V. I., Offermann, D., French,
712 W. J. R., Shepherd, M. G., Semenov, A. I., Remsberg, E. E., She, C. Y., Lübken, F. J., Bremer, J., Clemesha, B. R.,
713 Stegman, J., Sigernes, F., and Fadnavis, S.: Review of mesospheric temperature trends, *Rev. Geophys.*, 41,
714 <https://doi.org/10.1029/2002RG000121>, 2003.
- 715 Beig, G., Scheer, J., Mlynczak, M. G., and Keckhut, P.: Overview of the temperature response in the mesosphere and
716 lower thermosphere to solar activity, *Rev. Geophys.*, 46, <https://doi.org/10.1029/2007RG000236>, 2008.
- 717 Dalin, P., Perminov, V., Pertsev, N., and Romejko, V.: Updated Long-Term Trends in Mesopause Temperature,
718 Airglow Emissions, and Noctilucent Clouds, *J. Geophys. Res. Atmos.*, 125, 1–19,
719 <https://doi.org/10.1029/2019JD030814>, 2020.
- 720 Das, U.: Spatial variability in long-term temperature trends in the middle atmosphere from SABER/TIMED
721 observations, *Adv. Sp. Res.*, 68, 2890–2903, <https://doi.org/10.1016/j.asr.2021.05.014>, 2021.
- 722 Dawkins, E. C. M., Feofilov, A., Rezac, L., Kutepov, A. A., Janches, D., Höffner, J., Chu, X., Lu, X., Mlynczak, M. G.,
723 and Russell, J.: Validation of SABER v2.0 operational temperature data with ground-based lidars in the
724 mesosphere-lower thermosphere region (75–105 km), *J. Geophys. Res. Atmos.*, 123, 9916–9934,
725 <https://doi.org/10.1029/2018JD028742>, 2018.
- 726 Domeisen, D. I. V., Garfinkel, C. I., and Butler, A. H.: The teleconnection of El Niño Southern Oscillation to the
727 stratosphere, *Rev. Geophys.*, 57, 5–47, <https://doi.org/10.1029/2018RG000596>, 2019.
- 728 Dunkerton, T.: On the mean meridional mass motions of the stratosphere and mesosphere, *J. Atmos. Sci.*, 35, 2325–
729 2333, [https://doi.org/10.1175/1520-0469\(1978\)035<2325:OTMMMM>2.0.CO;2](https://doi.org/10.1175/1520-0469(1978)035<2325:OTMMMM>2.0.CO;2), 1978.
- 730 Emmert, J. T., Drob, D. P., Picone, J. M., Siskind, D. E., Jones, M., Mlynczak, M. G., Bernath, P. F., Chu, X.,
731 Doornbos, E., Funke, B., Goncharenko, L. P., Hervig, M. E., Schwartz, M. J., Sheese, P. E., Vargas, F., Williams,
732 B. P., and Yuan, T.: NRLMSIS 2.0: a whole-atmosphere empirical model of temperature and neutral species
733 densities, *Earth Sp. Sci.*, 8, <https://doi.org/10.1029/2020EA001321>, 2021.
- 734 Forbes, J. M., Zhang, X., and Marsh, D. R.: Solar cycle dependence of middle atmosphere temperatures, *J. Geophys.*
735 *Res. Atmos.*, 119, 9615–9625, <https://doi.org/10.1002/2014JD021484>, 2014.
- 736 French, W. J. R., Mulligan, F. J., and Klekociuk, A. R.: Analysis of 24 years of mesopause region OH rotational
737 temperature observations at Davis, Antarctica – Part 1: long-term trends, *Atmos. Chem. Phys.*, 20, 6379–6394,
738 <https://doi.org/10.5194/acp-20-6379-2020>, 2020.
- 739 Gan, Q., Du, J., Fomichev, V. I., Ward, W. E., Beagley, S. R., Zhang, S., and Yue, J.: Temperature responses to the 11
740 year solar cycle in the mesosphere from the 31 year (1979–2010) extended Canadian Middle Atmosphere Model
741 simulations and a comparison with the 14 year (2002–2015) TIMED/SABER observations, *J. Geophys. Res. Sp.*
742 *Phys.*, 122, 4801–4818, <https://doi.org/10.1002/2016JA023564>, 2017.
- 743 Garcia, R. R. and Solomon, S.: The effect of breaking gravity waves on the dynamics and chemical composition of the
744 mesosphere and lower thermosphere., *J. Geophys. Res.*, 90, 3850–3868, <https://doi.org/10.1029/JD090iD02p03850>,
745 1985.

746 Garcia, R. R., Yue, J., and Russell, J. M.: Middle atmosphere temperature trends in the twentieth and twenty-First
747 centuries simulated with the Whole Atmosphere Community Climate Model (WACCM), *J. Geophys. Res. Sp.*
748 *Phys.*, 124, 7984–7993, <https://doi.org/10.1029/2019JA026909>, 2019.

749 Kutner, M., Neter, C. N. J., and Li, W.: *Applied linear statistical models*, 5th ed., McGraw-Hill Irwin, Boston, 1396 pp.,
750 2005.

751 Laštovička, J.: Global pattern of trends in the upper atmosphere and ionosphere: Recent progress, *J. Atmos. Solar-*
752 *Terrestrial Phys.*, 71, 1514–1528, <https://doi.org/10.1016/j.jastp.2009.01.010>, 2009.

753 Laštovička, J.: Progress in investigating long-term trends in the mesosphere, thermosphere, and ionosphere, *Atmos.*
754 *Chem. Phys.*, 23, 5783–5800, <https://doi.org/10.5194/acp-23-5783-2023>, 2023.

755 Laštovička, J. and Jelínek, Š.: Problems in calculating long-term trends in the upper atmosphere, *J. Atmos. Solar-*
756 *Terrestrial Phys.*, 189, 80–86, <https://doi.org/10.1016/j.jastp.2019.04.011>, 2019.

757 Laštovička, J., Akmaev, R. A., Beig, G., Bremer, J., and Emmert, J. T.: Global Change in the Upper Atmosphere,
758 *Science (80-.)*, 314, 1253–1254, <https://doi.org/10.1126/science.1135134>, 2006.

759 Li, T., Calvo, N., Yue, J., Dou, X., Russell, J. M., Mlynczak, M. G., She, C. Y., and Xue, X.: Influence of El Niño-
760 Southern oscillation in the mesosphere, *Geophys. Res. Lett.*, 40, 3292–3296, <https://doi.org/10.1002/grl.50598>,
761 2013.

762 Li, T., Calvo, N., Yue, J., Russell, J. M., Smith, A. K., Mlynczak, M. G., Chandran, A., Dou, X., and Liu, A. Z.:
763 Southern Hemisphere summer mesopause responses to El Niño-Southern Oscillation, *J. Clim.*, 29, 6319–6328,
764 <https://doi.org/10.1175/JCLI-D-15-0816.1>, 2016.

765 Li, T., Yue, J., Russell, J. M., and Zhang, X.: Long-term trend and solar cycle in the middle atmosphere temperature
766 revealed from merged HALOE and SABER datasets, *J. Atmos. Solar-Terrestrial Phys.*, 212, 105506,
767 <https://doi.org/10.1016/j.jastp.2020.105506>, 2021.

768 Liu, X., Yue, J., Xu, J., Garcia, R. R., Russell, J. M., Mlynczak, M., Wu, D. L., and Nakamura, T.: Variations of global
769 gravity waves derived from 14 years of SABER temperature observations, *J. Geophys. Res. Atmos.*, 122, 6231–
770 6249, <https://doi.org/10.1002/2017JD026604>, 2017.

771 Lübken, F. J., Berger, U., and Baumgarten, G.: On the anthropogenic impact on long-term evolution of noctilucent
772 clouds, *Geophys. Res. Lett.*, 45, 6681–6689, <https://doi.org/10.1029/2018GL077719>, 2018.

773 Lübken, F. J., Baumgarten, G., and Berger, U.: Long term trends of mesospheric ice layers: A model study, *J. Atmos.*
774 *Solar-Terrestrial Phys.*, 214, 105378, <https://doi.org/10.1016/j.jastp.2020.105378>, 2021.

775 Mlynczak, M. G., Daniels, T., Hunt, L. A., Yue, J., Marshall, B. T., Russell, J. M., Remsberg, E. E., Tansock, J., Esplin,
776 R., Jensen, M., Shumway, A., Gordley, L., and Yee, J. H.: Radiometric stability of the SABER instrument, *Earth*
777 *Sp. Sci.*, 7, 1–8, <https://doi.org/10.1029/2019EA001011>, 2020.

778 Mlynczak, M. G., Hunt, L. A., Garcia, R. R., Harvey, V. L., Marshall, B. T., Yue, J., Mertens, C. J., and Russell, J. M.:
779 Cooling and contraction of the mesosphere and lower thermosphere from 2002 to 2021, *J. Geophys. Res. Atmos.*,
780 127, 1–17, <https://doi.org/10.1029/2022JD036767>, 2022.

781 Mlynczak, M. G., Marshall, B. T., Garcia, R. R., Hunt, L., Yue, J., Harvey, V. L., Lopez-Puertas, M., Mertens, C., and
782 Russell, J.: Algorithm stability and the long-term geospace data record from TIMED/SABER, *Geophys. Res. Lett.*,
783 50, 1–7, <https://doi.org/10.1029/2022GL102398>, 2023.

784 Qian, L., Burns, A., and Yue, J.: Evidence of the lower thermospheric winter-to-summer circulation from SABER CO2
785 observations, *Geophys. Res. Lett.*, 44, 10,100-10,107, <https://doi.org/10.1002/2017GL075643>, 2017.

786 Qian, L., Jacobi, C., and McInerney, J.: Trends and solar irradiance effects in the mesosphere, *J. Geophys. Res. Sp.*
787 *Phys.*, 124, 1343–1360, <https://doi.org/10.1029/2018JA026367>, 2019.

788 Ramesh, K., Smith, A. K., Garcia, R. R., Marsh, D. R., Sridharan, S., and Kishore Kumar, K.: Long-term variability and
789 tendencies in middle atmosphere temperature and zonal wind from WACCM6 simulations during 1850–2014, *J.*
790 *Geophys. Res. Atmos.*, 125, <https://doi.org/10.1029/2020JD033579>, 2020.

791 Randel, W. J., Garcia, R. R., Calvo, N., and Marsh, D.: ENSO influence on zonal mean temperature and ozone in the

792 tropical lower stratosphere, *Geophys. Res. Lett.*, 36, n/a-n/a, <https://doi.org/10.1029/2009GL039343>, 2009.

793 Remsberg, E. E., Marshall, B. T., Garcia-Comas, M., Krueger, D., Lingenfelter, G. S., Martin-Torres, J., Mlynczak, M.
794 G., Russell, J. M., Smith, A. K., Zhao, Y., Brown, C., Gordley, L. L., Lopez-Gonzalez, M. J., Lopez-Puertas, M.,
795 She, C. Y., Taylor, M. J., and Thompson, R. E.: Assessment of the quality of the version 1.07 temperature-versus-
796 pressure profiles of the middle atmosphere from TIMED/SABER, *J. Geophys. Res. Atmos.*, 113, 1–27,
797 <https://doi.org/10.1029/2008JD010013>, 2008.

798 Rezac, L., Kutepov, A., Russell, J. M., Feofilov, A. G., Yue, J., and Goldberg, R. A.: Simultaneous retrieval of T(p) and
799 CO₂ VMR from two-channel non-LTE limb radiances and application to daytime SABER/TIMED measurements,
800 *J. Atmos. Solar-Terrestrial Phys.*, 130–131, 23–42, <https://doi.org/10.1016/j.jastp.2015.05.004>, 2015.

801 Russell, J. M., Bailey, S. M., Gordley, L. L., Rusch, D. W., Horányi, M., Hervig, M. E., Thomas, G. E., Randall, C. E.,
802 Siskind, D. E., Stevens, M. H., Summers, M. E., Taylor, M. J., Englert, C. R., Espy, P. J., McClintock, W. E., and
803 Merkel, A. W.: The Aeronomy of Ice in the Mesosphere (AIM) mission: Overview and early science results, *J.*
804 *Atmos. Solar-Terrestrial Phys.*, 71, 289–299, <https://doi.org/10.1016/j.jastp.2008.08.011>, 2009.

805 She, C. Y., Berger, U., Yan, Z., Yuan, T., Lübken, F. -J., Krueger, D. A., and Hu, X.: Solar response and long-term
806 trend of midlatitude mesopause region temperature based on 28 years (1990–2017) of Na lidar observations, *J.*
807 *Geophys. Res. Sp. Phys.*, 124, 7140–7156, <https://doi.org/10.1029/2019JA026759>, 2019.

808 Tapping, K. F.: The 10.7 cm solar radio flux (F 10.7), *Sp. Weather*, 11, 394–406, <https://doi.org/10.1002/swe.20064>,
809 2013.

810 Venkat Ratnam, M., Akhil Raj, S. T., and Qian, L.: Long-term trends in the low-latitude middle atmosphere
811 temperature and winds: observations and WACCM-X model simulations, *J. Geophys. Res. Sp. Phys.*, 124, 7320–
812 7331, <https://doi.org/10.1029/2019JA026928>, 2019.

813 Wang, N., Qian, L., Yue, J., Wang, W., Mlynczak, M. G., and Russell, J. M.: Climatology of mesosphere and lower
814 thermosphere residual circulations and mesopause height derived from SABER observations, *J. Geophys. Res.*
815 *Atmos.*, 127, 1–14, <https://doi.org/10.1029/2021JD035666>, 2022.

816 Xu, J., Liu, H.-L., Yuan, W., Smith, A. K., Roble, R. G., Mertens, C. J., Russell, J. M., and Mlynczak, M. G.:
817 Mesopause structure from Thermosphere, Ionosphere, Mesosphere, Energetics, and Dynamics (TIMED)/Sounding
818 of the Atmosphere Using Broadband Emission Radiometry (SABER) observations, *J. Geophys. Res.*, 112, D09102,
819 <https://doi.org/10.1029/2006JD007711>, 2007.

820 Yu, W., Garcia, R., Yue, J., Smith, A., Wang, X., Randel, W., Qiao, Z., Zhu, Y., Harvey, V. L., Tilmes, S., and
821 Mlynczak, M.: Mesospheric temperature and circulation response to the Hunga Tonga-Hunga-Ha’apai volcanic
822 eruption, *J. Geophys. Res. Atmos.*, 128, 1–10, <https://doi.org/10.1029/2023JD039636>, 2023.

823 Yuan, T., Solomon, S. C., She, C. -Y., Krueger, D. A., and Liu, H. -L.: The long-term trends of nocturnal mesopause
824 temperature and altitude revealed by Na lidar observations between 1990 and 2018 at midlatitude, *J. Geophys. Res.*
825 *Atmos.*, 124, 5970–5980, <https://doi.org/10.1029/2018JD029828>, 2019.

826 Yue, J., Russell, J., Jian, Y., Rezac, L., Garcia, R., López-Puertas, M., and Mlynczak, M. G.: Increasing carbon dioxide
827 concentration in the upper atmosphere observed by SABER, *Geophys. Res. Lett.*, 42, 7194–7199,
828 <https://doi.org/10.1002/2015GL064696>, 2015.

829 Yue, J., Russell, J., Gan, Q., Wang, T., Rong, P., Garcia, R., and Mlynczak, M.: Increasing water vapor in the
830 stratosphere and mesosphere after 2002, *Geophys. Res. Lett.*, 46, 13452–13460,
831 <https://doi.org/10.1029/2019GL084973>, 2019a.

832 Yue, J., Li, T., Qian, L., Lastovicka, J., and Zhang, S.: Introduction to special issue on “Long-term changes and trends
833 in the middle and upper atmosphere,” *J. Geophys. Res. Sp. Phys.*, 124, 10360–10364,
834 <https://doi.org/10.1029/2019JA027462>, 2019b.

835 Zhang, S., Cnossen, I., Laštovička, J., Elias, A. G., Yue, X., Jacobi, C., Yue, J., Wang, W., Qian, L., and Goncharenko,
836 L.: Long-term geospace climate monitoring, *Front. Astron. Sp. Sci.*, 10, 1–5,
837 <https://doi.org/10.3389/fspas.2023.1139230>, 2023.

838 Zhao, X. R., Sheng, Z., Shi, H. Q., Weng, L. B., and Liao, Q. X.: Long-term trends and solar responses of the
839 mesopause temperatures observed by SABER during the 2002–2019 period, *J. Geophys. Res. Atmos.*, 125, 1–17,
840 <https://doi.org/10.1029/2020JD032418>, 2020.

841 Zhao, X. R., Sheng, Z., Shi, H. Q., Weng, L. B., and He, Y.: Middle atmosphere temperature changes derived from
842 SABER observations during 2002-2020, *J. Clim.*, 34, 1, <https://doi.org/10.1175/JCLI-D-20-1010.1>, 2021.

843